Vilnius University
Faculty of Physics
Institute of Photonics and Nanotechnology

The miEye: a Bench-top Cost-effective Super-resolution Single-Molecule Localization Microscope

Master Thesis
Photonics and Nanotechnology study programme

Student: Mohammad Nour Alsamsam

Academic supervisor: dr. Marijonas Tutkus

Vilnius 2023

Contents

1 Introduction **2**

2 Literature Review **3**
2.1 Resolution of an Optical System . . . 3
2.2 Contrast Enhancement Techniques . . . 4
2.3 Selective Plane Illumination Microscopy . . . 5
2.4 Super Resolution Microscopy . . . 6

3 Research Methodology **9**
3.1 Experimental Setup . . . 9
3.2 Dark Sensor Measurement . . . 11
3.3 Data Analysis . . . 12
3.4 CMOS Sensors . . . 13
3.4.1 Camera Cooling . . . 14
3.5 Samples . . . 15
3.5.1 ATTO647N Dye Sandwich . . . 15
3.5.2 GATTA-PAINT nano-rulers . . . 15
3.5.3 U-2 OS Cells with Labelled Nup96 Complexes . . . 16

4 Results and Discussion **17**
4.1 CMOS Characterization . . . 17
4.2 Excitation Profiles . . . 18
4.3 Gatta-PAINT . . . 20
4.4 dSTORM Imaging . . . 22

5 Conclusions **23**

6 Summary **24**

7 Acknowledgement **25**

8 Supplementary Materials **30**

1 Introduction

Commercial single-molecule localization microcopy (SMLM) microscopes with dedicated hardware and software are generally expensive, hard to modify at demand, and maintenance or expansion modules are offered at a premium. Consequently, in many laboratories, super-resolution microscopy setups are custom-made utilizing commercially available microscope bodies[1]. Lab-made setups on the other hand are indefinitely adjustable but require qualified staff and custom-made software for hardware control, data acquisition and analysis due to the lack of a universal open source solution. Various open-source initiatives from innovative researchers sharing their super-resolution microscopy setups are readily available on different repositories[2]. Notable SMLM approaches include: cellSTORM[3, 4], easySTORM[5], K2 TIRF[6], lifeHack[7], liteTIRF[8], LSFM[9], miCube [10, 11]. Cost-effective solutions for various components including light sources, and detectors are not implemented in all of these examples. The general shortcomings of those systems are related to insufficient documentation, compatibility with open-source software, and extremely time-consuming technical support, which is typically not incentivized by the present financing and publication environment.

In the past, active pixel complementary metal-oxide semiconductor (CMOS) sensors were not a practical alternative to charge-coupled device (CCD) sensors for scientific applications due to their low quantum efficiency (QE) and high readout noise. However, recent advancements in back-illuminated scientific-CMOS (sCMOS) cameras have resulted in peak QE up to 95%, high readout speeds, and low noise. Unlike electron multiplying CCDs (EMCCDs), sCMOS cameras do not suffer from charge multiplication noise, which reduces the actual QE. As a result, sCMOS eliminates the trade-off between acquisition speed and sensitivity while offering larger detector array sizes. Additionally, some CMOS detectors have implemented the global shutter regime, which eliminates spatial distortion, an unavoidable artifact for rolling shutter cameras[12]. This feature is particularly important for dynamic imaging applications where accurate representation of motion is crucial. Scientific detectors, such as sCMOS and EMCCD, are expensive, costing around ∼€10–30k, which can make them challenging to acquire for budget-limited research. However, one should note that the objective is the most important item and costs more than €10k. Therefore, it is not worth making any compromises on it. We believe that compromising the detector would not result in significant impacts, like introducing aberrations or artifacts. Furthermore, commercial monochromatic CMOS cameras are typically optimized for visible wavelengths, resulting in decreased sensitivity at longer wavelengths where their peak QE lies in the blue-green spectral region.

Recently, technological advancements have led to the development of cost-effective (≤€1k) back-illuminated industrial CMOS (iCMOS) cameras with peak QE up to 80% and low readout noise around 2.1 e^- [13]. To ensure optimal performance, it is important to carefully address the issues associated with iCMOS solutions. One drawback of iCMOS is its reliance on passive cooling, which can result in increased dark current and thermal noise values. Additionally, unlike sCMOS, there is currently no reliable software available for iCMOS that is specifically designed for SMLM acquisition. While introducing CMOS for single molecule localization microscopy (SMLM) is promising, it requires accounting for pixel-wise readout noise in the data analysis pipeline, which has already been addressed[14]. Efforts to implement iCMOS have been investigated, but early versions suffered from low QE and high readout noise[15].

The development of dedicated software for hardware control, data acquisition, and analysis for super-resolution microscopy is rapidly progressing under open-source licenses. However, commercial solutions such as Nikon's NIS elements are available but can be expensive and are not compatible with home-built hardware. Solutions are typically implemented using programming languages or environments such as MATLAB, LabView, C, Java or even Python and a summary of available solutions is found on the open microscopy repository[2]. ImageJ[16],

a Java-based scientific image processing program, and FiJi[17], a subsequent distribution devoted for biological image analysis, are widely used and well documented. Moreover, Napari, a multi-dimensional image viewer for Python[18], is becoming more popular as a tool for viewing, annotating, and analyzing large multi-dimensional datasets. Free software dedicated for super resolution data analysis is widely spread across different platforms such as: SMAP[19], a MATLAB modular platform with hundreds of plugins, ThunderSTORM[20], QuickPALM[21], as ImageJ plugins, RapidSTORM[22], Localizer[23], dedicated software written in C++, and Picasso[24] a Python package. Yet, typically in many cases the software is not maintained as the development stops at a certain point and adding additional algorithms in all cases can be challenging. The μManager plugin for ImageJ makes it simple to integrate data acquisition and analysis[25]. μManager is a framework for computer control of microscopes, cameras, stages, and other auxiliary equipment from a wide range of manufacturers. However, μManager lacks the documentation for developers and has a high entry barrier for implementing new hardware device adapters written in C++ among other software bugs and frequent crashes. There is a need for a reliable turn-key software in the biophysics and biology community that would enable researchers to concentrate on sample preparation and biological discoveries instead of dealing with software and hardware issues. The growing interest of the scientific community in Python is generally due to its simplicity and low entry barrier which makes it an ideal choice especially when combined with performance optimized algorithms.

In this work, we introduce the *miEye*, a bench-top cost-effective (∼€50k) super-resolution single-molecule localization microscope, already published by the author[26]. The *miEye* is accompanied by the *microEye* Python package, which provides hardware control, data acquisition, and analysis capabilities[27]. The *miEye* utilizes industrial CMOS cameras with thermoelectric and water cooling to achieve a high signal-to-noise ratio (SNR) for single-molecule detection. We employ a dark calibration approach to characterize pixel-wise offset and variance, which is incorporated into an iterative Levenberg–Marquardt maximum-likelihood estimate (MLE) algorithm for localizing single emitters through 2D Gaussian fitting[28, 29]. We evaluate the excitation profiles for the different interchangeable configurations of the *miEye*. Additionally, we benchmark the microscope's stability and achievable resolution by performing DNA points accumulation for imaging in nanoscale topography (DNA-PAINT) imaging of a commercially available nano-rulers sample. We intend to complement the DNA-PAINT results by using an in-lab prepared sample for direct stochastic optical reconstruction microscopy (dSTORM) imaging of nuclear pore complexes (NPCs) in U2OS cells.

The aim of this work is to design and build an open-source bench-top super-resolution SMLM platform using cost-effective equipment, identify the optimal industrial CMOS camera, benchmark the performance of *miEye* using commercially available DNA-PAINT nano-rulers sample, assess its performance in dSTORM imaging of nuclear pore complexes, and create a robust platform for *miEye* using the Python open-source package *microEye*.

2 Literature Review

2.1 Resolution of an Optical System

The foundation describing the resolution of an optical imaging system was laid down by *Ernst Abbe* with his first publication in 1873[30, 31]. The resolving power was introduced as proportional to the wavelength of light λ and inversely proportional to the numerical aperture (NA) of the objective. Although, *Abbe*'s publications lacked the mathematical derivation of his theorem it was later provided after his passing by *O. Lummer* in 1910[32]. Imaging two-slits with a separation of $\Delta_{x,y} = \frac{\lambda}{2 \cdot \mathrm{NA}}$ showed an intensity dip between the two peaks, which was referred to as the resolving power limit of a microscope at the time[31]. Another definition, the

Rayleigh criterion introduced by physicist John William Strutt, 3rd Baron Rayleigh, is when the Airy pattern peak of one point emitter overlaps with the first minimum of the Airy pattern of the other[33, 34]. Moreover, Carrol Mason Sparrow defined a less commonly encountered resolution limit as the distance between two point emitters when the total point spread function (PSF) has no intensity dip at the midpoint and instead has an intensity plateau[35]. Figure 2.1 demonstrates a comparison between these previously described theoretical criteria. A more practical measure is the full width at half maximum (FWHM) of the PSF that can be easily evaluated in the lab by imaging a pseudo point emitter and the separation $\Delta_{x,y} = 0.51 \cdot \lambda/\mathrm{NA}$ is equal to the FWHM. Nevertheless, an imaging system's resolution is influenced by the quality of its optics, detection and display components, in addition to the nature of the input source radiation.

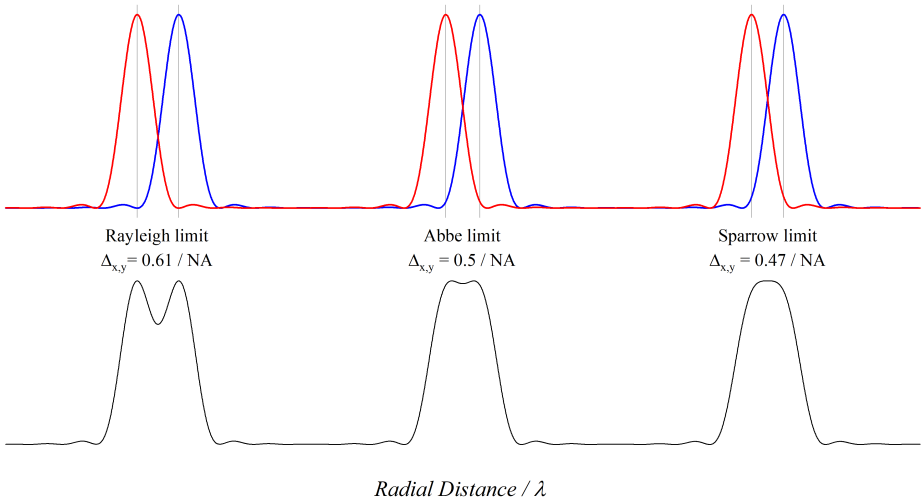

Fig. 2.1 A comparison of Rayleigh's, Abbe's and Sparrow's criteria for the lateral resolving power limit of an imaging system of two diffraction-limited point emitters.

2.2 Contrast Enhancement Techniques

Contrast enhancement techniques for microscopy developed drastically over the past such as: the transition from transmission to reflection imaging configurations, and the development of different specimen illumination and imaging modularities, e.g. dark-field, phase-contrast, differential interference contrast (DIC). Yet, such approaches do not improve the theoretical lateral resolution beyond the diffraction limit. Moreover, in optical microscopy, the axial resolution is worse than the lateral one due to the elliptical PSF and is in the order of $\Delta_z = 2 \cdot \lambda/\mathrm{NA}^2$. Conventional wide-field fluorescence microscopy suffer from the out-of-focus light that contributes as image background reducing the contrast of images, although the brightest and highest intensities are at the focal plane of the objective. Confocal microscopy enhances the resolution by exciting a single diffraction-limited spot and then by physically blocking the out-of-focus light using a pin-hole aperture only the light emitted from the desired focal spot passes through to the detector[36]. Figure 2.2 illustrates the aforementioned in-focus and out-of-focus light propagation schemes in a confocal microscope. However, confocal microscopy configuration requires raster scanning of the sample, either by moving it or the laser beam, to acquire a certain field of view and allows for features such as adjustable magnification and 3D imaging. Most common confocal configurations are laser scanning and spinning disk confocal microscopy. The minimum resolvable distance between two points in the lateral plane of the confocal microscope

is approximated as $\Delta_{x,y} \approx 0.4 \cdot \lambda/\text{NA}$, whereas the axial resolution is $\Delta_z \approx 1.4 \cdot \lambda \cdot n/\text{NA}^2$ where n is the refractive index of the immersion medium[37]. Factors such as the zoom effect and scanning speed affect the resolution, and the detector's signal-to-noise ratio (SNR) limits the imaging depth within a specific sample.

Exploiting optical non-linear effects in multi-photon microscopes allowed enhancing the resolution of confocal microscopy, achieve minimal photobleaching, and greater imaging depths[36]. Multi-photon excitation, typically 800-900 nm, is confined in a drastically smaller volume and IR light is less scattered and absorbed than visible light especially that the scattered IR light is too weak to excite fluorescence. For two-photon microscopy, the resolution is estimated to be laterally $\Delta_{x,y} = 0.325 \cdot \lambda/(\sqrt{2} \cdot \text{NA}^{0.91})$ and axially $\Delta_z = (0.532 \cdot \lambda/\sqrt{2}) \cdot (1/(n^2 - \sqrt{n^2 - \text{NA}^2}))$ where NA is greater than 0.7[37]. Other super resolution schemes that expand on the confocal setting will be overviewed later in this chapter.

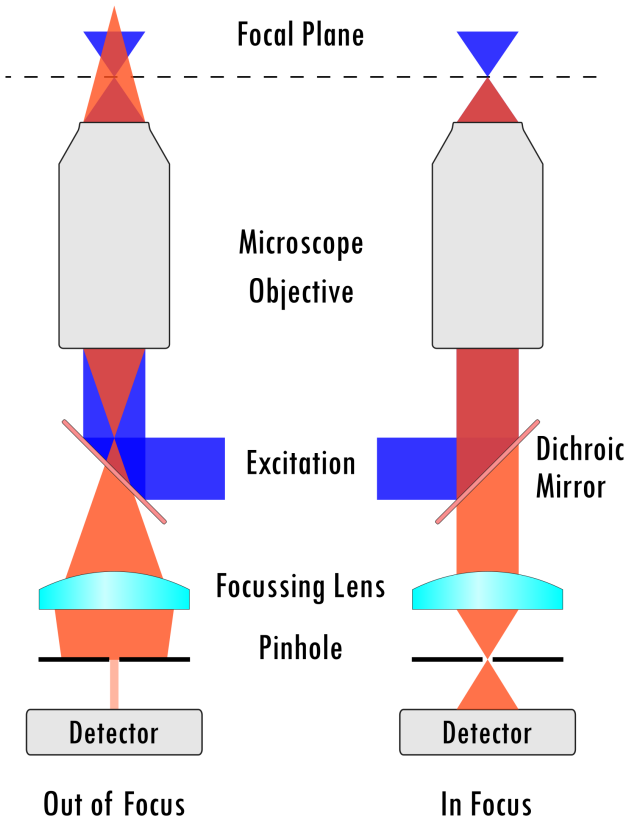

Fig. 2.2 The in-focus and out-of-focus light propagation schemes in a confocal microscope.

2.3 Selective Plane Illumination Microscopy

Improving the axial resolution for visible light microscopy can be challenging, thus we will review few solutions that were developed for this purpose. Total internal reflection fluorescence (TIRF) configuration uses a collimated oblique excitation that is totally reflected at the interface between the immersion medium and typically the glass cover-slip on which the sample is fixated. This setting results in a penetrating evanescent field which depth can be adjusted by increasing the incident angle of excitation at the interface. Thus, the TIRF evanescent field exponentially decays within a small distance above the interface (Figure 2.3A) and typically can excite molecules within $\sim 100 - 200$ nm[38]. However, TIRF microscopy requires high NA

immersion type objectives and is restricted to a small field of view (FOV) and set of specificity prepared samples. In contrast with TIRF, light sheet fluorescence (LSF) microscopy enables imaging a narrow slice deep within the sample by exciting the volume orthogonally using a light sheet. The excitation is an elliptical beam produced by introducing a cylindrical lens into the Gaussian excitation beam's path then orthogonally superimposed with the detection's FOV using a low NA objective, typically water immersion. This enables detecting fluorescence from a thickness equal to the total beam width along the z-axis ($2 \cdot \omega_z$) with a FOV approximately estimated as twice the Rayleigh length (z_r) as illustrated in Figure 2.3B[39]. However, one-sided LSF excitation battles with stripe patterns in acquired images due to sample absorption that creates the stripe-shaped shadows hindering image post-processing and interpretation. One solution is the introduction of double-sided excitation with two oppositely propagating light sheets minimizing shadowing effects as shown in Figure 2.3C where the two beams are misaligned for demonstrative purposes. LSF microscopy allows for volumetric imaging with its detection depth being limited by light scattering, absorption, and sample-induced aberrations along with the excitation broadening, path deviation and attenuation.

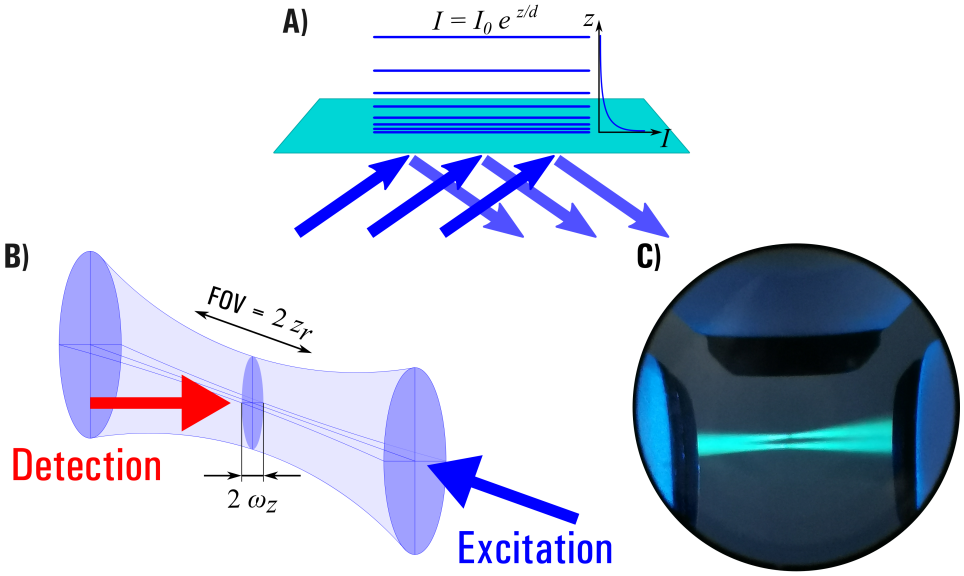

Fig. 2.3 A) The TIRF exponentially decaying evanescent field excitation. B) LSF microscopy scheme with one-sided excitation depth and detection FOV illustrated. C) Double-sided LSF showing two light sheets that are misaligned for demonstrative purposes.

2.4 Super Resolution Microscopy

Structured illumintation microscopy (SIM) is a wide-field super-resolution approach that expands the resolution twice beyond the diffraction limit of conventional microscopy by exploiting moiré fringes (Figure 2.4A) produced by illuminating the sample with a line patterned excitation[40]. Looking at the reciprocal space in (Figure 2.4B), a conventional microscope is limited by the spatial cut-off frequency typically referred to as the diffraction limit and any information beyond it is unattainable. Due to this limit as well, a sinusoidal line pattern illumination, represented by three Fourier components in the reciprocal space, is limited by the same cut-off frequency (Figure 2.4C). The acquired moiré fringes hold extended information in reciprocal space corresponding to movement equal to the illumination's Fourier components as illustrated in Figure 2.4D. Thus acquiring 3 or more sample images with different illumination phase one could arithmetically deduce the aforementioned three components. Finally, by acquiring a set of these images at different illumination pattern orientation and phase the recovered information in reciprocal space is twice the size of a conventional microscope (Figure 2.4E), hence the

resolution is enhanced by a factor of two.

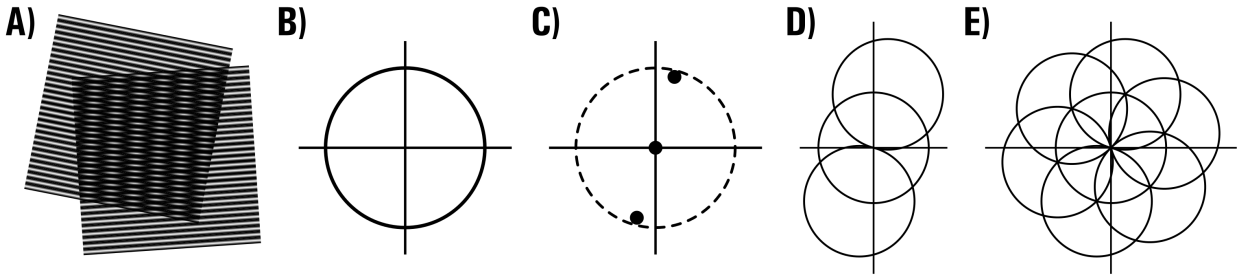

Fig. 2.4 A) Moiré fringes produced by multiplying two line patterns. B) The diffraction-limited conventional microscopy case where the cut-off spatial frequency in the reciprocal space is represented by the circle. C) The three Fourier components of a sinusoidal line pattern limited by the same cut-off frequency (dashed circle). D) Represents the extended information in reciprocal space acquired from the moiré fringes corresponding to movement equal to the illumination's Fourier components. E) A sequence of images acquired at different illumination pattern orientation and phase allows recovering information from an area twice the size of the conventional one.

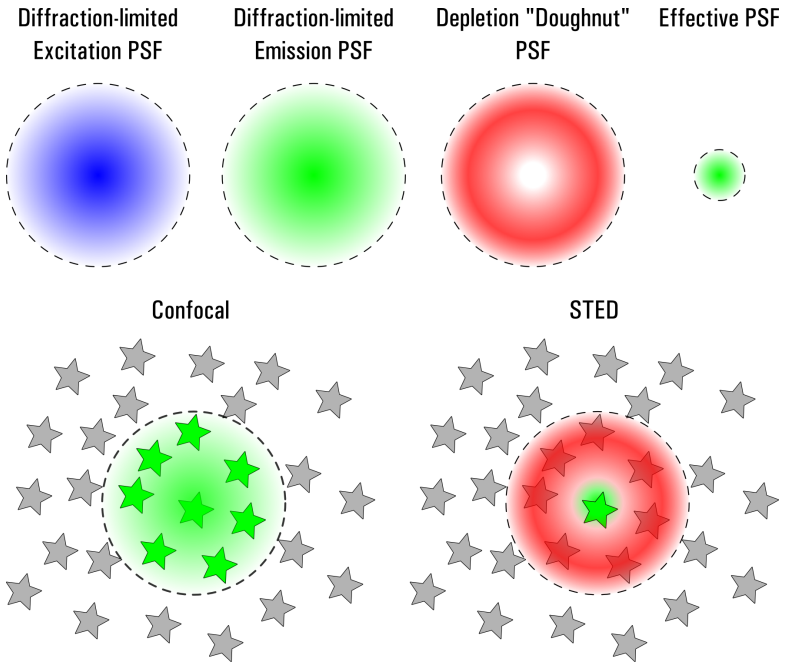

Fig. 2.5 A comparison of diffraction-limited confocal and STED microscopy, where the latter provides a sub-diffractional effective PSF as the depletion beam restricts spontaneous emission outside the zero central region.

Stimulated emission depletion (STED) super-resolution microscopy is a confocal setting where a Bessel doughnut-shaped depletion beam is used to prohibit spontaneous emission in fluorescent molecules — as the name suggests — by inducing stimulated emission[41, 42]. STED principle relies on the fact that fluorescence is detected only from within the central region of the depletion beam where destructive interference occurs (Figure 2.5). Thus, fluorescence is localized within a region of sub-diffractional dimensions and using deconvolution techniques the super-resolution images are produced. For STED to work, the stimulated emission rate of the fluorescent molecule should be higher than the rate of its spontaneous emission. The resolution of STED microscopy can go down to $\sim$ 20 nm[43], and is limited by the SNR which depends

on the detection efficiency, the fluorophore's brightness and photostability, and intensity distributions of the beams at the focal spot[44]. Third of the Nobel Prize in Chemistry 2014 was received by *Stefan W. Hell* for the development of STED microscopy in 2000[45]. Furthermore, a similar method called MINimal photon FLUXes (MINFLUX) has been developped and is capable of achieving $\sim 1-3$ nm of three-dimensional resolution[46, 47]. First, to achieve optimal molecular separation, MINFLUX switches on emitters one at a time. Second, MINFLUX uses an excitation beam that has a central intensity zero instead of a maximum reducing the number of detected photons. Performing a sequence of sub-nanometer probing scans, the intensity-zero beam localizes an emitting molecule by detecting reduced fluorescence. This approach enables high localization precision and even 3D single-molecule trajectory tracking in living cells[48].

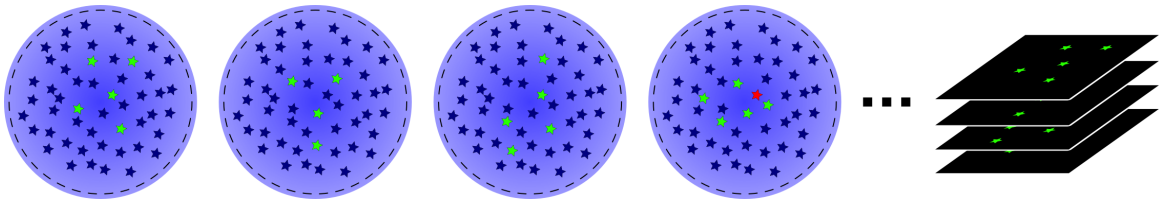

Fig. 2.6 PALM acquisition process under excitation beam and activation pulse, dark navy molecule are in reversible dark state, green ones are activated emitting molecules and red ones are photobleached in an irreversible dark state.

Moreover, the research on photoactivatable fluorescent proteins by *William E. Moerner* was awarded a third of the Nobel Prize in Chemistry 2014 where he engineered a variant of the green fluorescent protein (GFP) that could be reactivated by 405 nm light after its fluorescence fades under 488 nm excitation[45, 49]. Research on such fluorescent proteins facilitated the development of wide-field super-resolution single-molecule localization microcopy (SMLM) where emitters spatially separated by a distance larger than the diffraction limit and temporally seperated by on/off blinking events can be localized with nanometric precision. The first approach incorporating on/off blinking events to attain super-resolution called photoactivated localization microscopy (PALM) developped by *Eric Betzig* was awarded a third of the Nobel Prize in Chemistry 2014[45, 50, 51]. The PALM experiment is depicted in Figure 2.6, in which UV-activated molecules excited by a different wavelength emit until they fade into a reversible or irreversible dark state, and the acquisition cycle of activation, imaging and bleaching continues until sufficient blinking events to reconstruct a meaningful image are collected. Photoactivatable fluorescent proteins suffer from low photo-stability and brightness, thus PALM experiments has to be carefully engineered but due to their small size they can yield higher resolution images compared with other SMLM techniques. Photoactivatable fluorescent proteins are endogenously produced in cells and organelles and genetically fused to target proteins. Also, stable cell lines can be produced with protein-labeling efficiencies close to 100%, a threshold that chemical staining with synthetic fluorophores is unable to attain[52].

Stochastic optical reconstruction microscopy (STORM) is another SMLM technique that uses photo-switchable dye-pairs to achieve the temporal separation of fluorophore emission by on/off blinking[53]. STORM requires two laser wavelengths one of them with high power density to achieve photo-switching, and compromises resolution due to its larger label size of the dye-pair labelled antibodies. In addition, direct stochastic optical reconstruction microscopy (dSTORM) was developed using a single organic fluorescent dye, where the number of active fluorophores is optimized to be spatially separated at distances greater than the diffraction limit by varying the laser intensity, thiol, and oxygen concentrations[52, 54]. The OFF state lifetime typically can range from 100 ms to several seconds after irradiation with excitation densities low enough not cause permanent photobleaching. Another method called DNA points accumulation for imaging in nanoscale topography (DNA-PAINT) utilizes the transient bind-

ing of short dye-labelled "imager" oligonucleotides to a complimentary target "docking" strands creating the required blinking for super-resolution single-molecule localization imaging[24]. The imager strand is conjugated to an organic dye and freely diffuses in the imaging buffer, where docking strands are fixed to a biological target of interest as in Figure 2.7A. Although Imager strands create a background as they diffuse over various camera pixels during single frame acquisition, when transiently bound to a specific docking strand the photons sufficiently accumulate for single-molecule detection. DAN-PAINT facilitates spectrally unlimited multiplexing with programmable and specific DNA molecules allowing blinking independently from the dye photophysics. As a benchmarking and calibration tool for DNA-PAINT based super-resolution SMLM, complex and arbitrary shaped nanostructures are fabricated using the DNA origami technology[55]. Figure 2.7B demonstrates a nanorod fabricated with three docking positions that is typically used for the assessment of SMLM system precision and resolution where the distances between targets d_1 and d_2 are predefined by design.

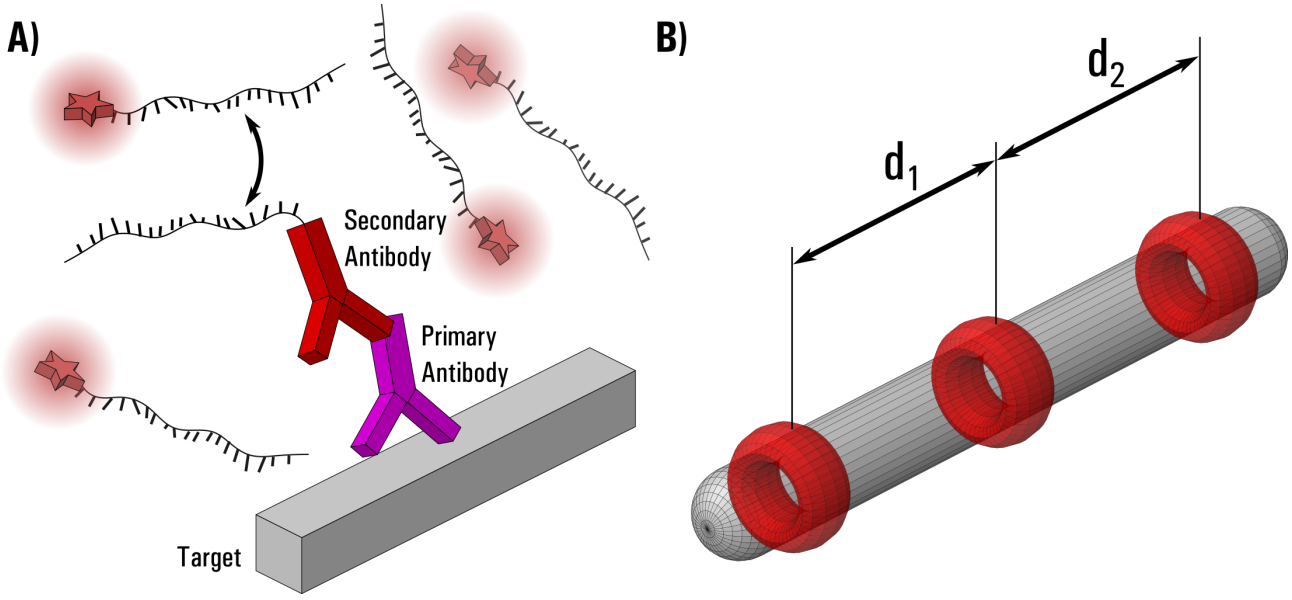

Fig. 2.7 A) DNA-PAINT technology labelling that illustrates imager strands diffusing in buffer and a docker strand located at the targetted feature where transient or permanent binding can occur. B) A nanorod fabricated using DNA origami with three docking positions where d_1 and d_2 are engineered on design to be equal or different.

3 Research Methodology

3.1 Experimental Setup

We utilize the *miEye*, a modular super-resolution single-molecule localization fluorescence microscope, for our investigations [26]. The *miEye* is a variant of the miCube [11]. The microscope's excitation is provided by a controllable laser diode combiner (Integrated Optics) with four laser diodes emitting at 405 nm, 488 nm, 520 nm, and 638 nm wavelengths. The laser output is coupled into either a polarization-maintaining single-mode fiber (SMF) or a square-core multi-mode fiber (MMF). The laser coupling into the SMF (P1-405BPM-FC-1, Thorlabs) is achieved using a 40X objective mounted onto an XY differential translator (ST1XY-D/M, Thorlabs), where the free-space beam is guided using a set of two silver-coated mirrors. The SMF output is collimated using an aspheric lens (CFC8-A, Thorlabs) and expanded using a telescope composed of two achromatic doublets. The epi-fluorescence illumination is realized by focusing the expanded beam onto the back focal plane (BFP) of the objective. A trans-

lation stage allows for moving the beam at BFP to produce HILO or TIRF illumination, as illustrated in Figure 3.1A. An iris diaphragm enables adjusting the field of illumination, and a 4-band laser-line excitation filter removes any autofluorescence produced by the fiber.

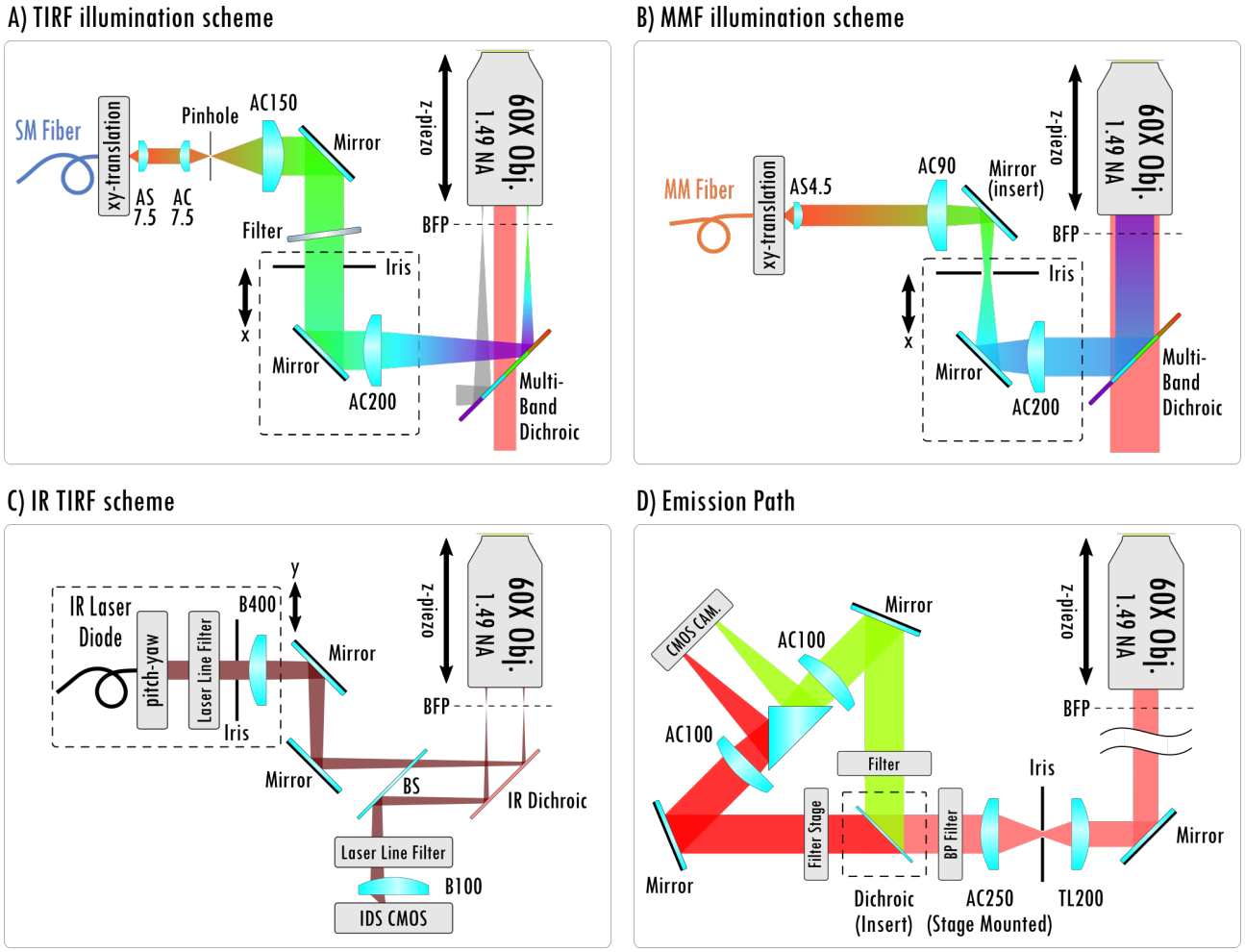

Fig. 3.1 The *miEye* microscope optical schematic displays the following components: A) TIRF SMF-based excitation, B) flat-field MMF-based illumination, C) IR TIRF focus locking, and D) dual emission detection paths. The components are labeled as follows: AC (Achromat), AS (Aspheric lens), BFP (Back focal plane), BS (Beam-splitter), TL (Tubelens), and V (Plano-convex-V-coated).

The MMF (M103L05) output is utilized for flat-field top-hat illumination. Here, the fiber end is a conjugate plane of the sample plane, with a selected magnification that matches the desired field of view or excitation power density, as shown in Figure 3.1B. In Figure 3.1C, the microscope achieves focus locking using an IR beam in a TIRF setting. The back-reflection of the IR beam from the sample interface is tracked using a CMOS camera (UI-3060CP-M, Imaging Development Systems). Subsequently, the z-piezo stage (FOC100, Piezo Concept) compensates for any drift along the optical axis and keeps the sample in focus using a closed loop configuration. The automatic focus stabilization functionality is implemented using a proportional loop in the *microEye* control module. The emission path, depicted in Figure 3.1D, allows for dual channel imaging on a single detector by adding an optional dichroic insert. After the objective, there is an expanding telescope with an iris acting as a field stop and a set of spectral filters suitable for different applications. The final achromatic lenses focus the view at the detector plane. It is recommended that the overall system magnification, or the so-called

projected pixel-size, be kept within the Nyquist limit for SMLM[1]. Note that for TIRF, a high NA objective is required to achieve total internal reflection. In our case, we use a 60X oil immersion Apochromat from Nikon with 1.49 NA.

3.2 Dark Sensor Measurement

For dark measurements, we capture a statistically sufficient amount of dark images such that the estimated pixel-wise mean μ_i and variance σ_i^2 are accredited to both (Eq. 3.1,3.2) for a given exposure time τ_{exp} and temperature T.

$$N_{i.\ dc} = I_{i,\ dc} \cdot \tau_{exp} + B_i, \tag{3.1}$$

$$\sigma^2_{i.\ rt} = \sigma^2_{i,\ thermal} \cdot \tau_{exp} + \sigma^2_{i,\ readout}, \tag{3.2}$$

where $N_{i,\ dc}$ is a pixel's dark current count, $I_{i,\ dc}$ is the dark current in [e$^-$ /(pixel·s)] or [ADU/(pixel·s)], B_i is the baseline, $\sigma^2_{i,\ rt}$ is the total readout noise variance, $\sigma_{i,\ thermal}$ is the thermal noise [e$^-$ /(pixel·$\sqrt{\text{s}}$)] and $\sigma_{i,\ readout}$ is the readout noise.

Furthermore, the pixel-wise inverse gain [e$^-$ /ADU] – the parameter that describes the number of generated photoelectrons [e$^-$] per signal unit count [ADU] – defined as[56]:

$$g_i = N_i/S_i \Rightarrow \frac{\text{Var}(N_i)}{N_i} = \frac{g_i^2 \cdot \text{Var}(S_i)}{g_i \cdot S_i} \Rightarrow \frac{\text{Var}(S_i)}{S_i} = \frac{1}{g_i}, \tag{3.3}$$

where N_i is the number of photo-induced or thermally-excited electrons and S_i is the measured signal counts in ADUs where one takes advantage of $N_i = \text{Var}(N_i)$ for paticles that follow a Poisson distribution. Information on iCMOS active and passive lab-made cooling is given in subsection (3.4.1). The CMOS firmware's built-in correction algorithms should be disabled in order to collect exclusively raw data for such measurements. For each given exposure time, the CMOS camera is initially operated until it reaches thermal equilibrium.

Capturing a large number of full sensor images and estimating the mean and variance maps requires both large storage space and computational power. We have developed an algorithm that computes the mean and variance maps simultaneously during data acquisition in order to save time and storage. That method evaluates the following mathematical expressions:

$$\mu_i = \frac{1}{n}\sum_{k=0}^{n-1} S_{i,k} \qquad [\text{ADU}], \tag{3.4}$$

$$\sigma_i^2 = \frac{1}{n-1}\left(\sum_{k=0}^{n-1} S_{i,k}^2 - \frac{1}{n}\left(\sum_{k=0}^{n-1} S_{i,k}\right)^2\right) \qquad [\text{ADU}^2]. \tag{3.5}$$

Acquiring different mean and variance maps at several exposure time values allows estimating the pixel-wise inverse gain mentioned in (Eq. 3.3) from:

$$\sigma_i^2(\tau_{exp}) = \frac{1}{g_i} \cdot \mu_i(\tau_{exp}) + \sigma_0^2. \tag{3.6}$$

Consequently, a linear fit of the pixel-wise variance dependency on its mean value at each assessed exposure time yields the gain as the slope. Our data in [ADU] is converted to photoelectrons [e$^-$] through a multiplication by the estimated inverse gain, allowing us to compare the investigated cameras performance. The linear least squares fitting of the pixel-wise mean and variance dependency on exposure time is employed to obtain an estimation of the pixel-wise dark current, baseline, thermal, and readout noise maps.

[1]Typically around half of the diffraction limit.

The aforementioned maps are used to generate offset and variance maps at any given exposure time, as well as sensor analysis tasks such as parameter distribution, uniformity, and detecting dead or hot pixels. Given a detector with m pixels one could also introduce the mean value of any parameter x as:

$$\bar{x} = \frac{1}{m} \sum_{i=0}^{m-1} x_i, \tag{3.7}$$

where we would refer to it a the parameter's mean not to be confused with the pixel-wise mean introduced earlier.

3.3 Data Analysis

To transform acquired images into a collection of preliminary localizations, simple detection algorithms of emitters are applied after image filtering and intensity threshold adjustment to identify specific features. Initially, image filters are applied, which can be spatial or temporal. Spatial filters use methods like the difference of Gaussians (DoG) or bandpass filtering, while temporal filters use approaches like the temporal median filter to eliminate noise and background effects. After selecting a relative intensity threshold, the image is passed into a simple blob detector included in the OpenCV library, which provides preliminary coordinates of emitters[57]. Then, regions of interest (ROIs) of $n \times n$ size around the central preliminary coordinates are collected for the final fitting procedure. Two approaches are implemented: a non-iterative phasor fit method[58] and a Newton and Levenberg–Marquardt iterative schemes for maximum likelihood estimation (MLE) fit[28]. The phasor fit converts the ROI around the point spread function (PSF) into Fourier domain and evaluates the two phase vectors of the first Fourier coefficients along the x and y directions. The algorithm is capable of predicting the lateral coordinates of a single emitter by estimating the angle of each phasor, and axial information is extracted from the ratio of phasor magnitudes for astigmatic PSFs. The phasor fit can be employed as an independent fitting procedure for accelerating the localization process or as a preliminary estimate for computationally intensive iterative approaches. The more preferable approach is the MLE scheme adapted into Python as *pyfit3Dcspline* a part of the *microEye* package[27], and implemented originally as *fit3Dcspline* into Matlab by *J. Ries et al.*[28]. It offers different methods including 2D Gaussian fitting for symmetrical and asymmetrical PSF models, and a 3D cspline fit of an experimentally generated PSF model specific to the microscope's optical setup. The algorithm is both CPU and GPU accelerated for optimized performance and generates Cramér–Rao lower bounds for uncertainty estimates, unlike the phasor fit.

Super-resolution images are typically produced by visualizing localizations in a 2D histogram of detected photon count in a certain bin width. However, SMLM localizations often suffer from out-of-focus drift, even when focus is locked, which can range from a few tens to hundreds of nanometers depending on the setup stability and experiment length. To improve the quality of super-resolution images, 2D or 3D drift correction based on cross-correlation algorithms can estimate the shift. The drift correction algorithm splits localizations into different time-bins, generates super-resolution images, and deduces the lateral shift from the phase difference in Fourier space. The estimated shift is then interpolated using a cubic spline function to determine single-frame drift. For kinetic experiments where the sample lacks any fixed features, fiducial markers can be introduced to provide more accurate drift evaluation compared with interpolation methods.

Fourier ring correlation (FRC) is a widely used method for determining the resolution of super-resolution images. FRC analysis involves calculating the correlation between two images, each generated from half of the data picked using a random binomial, and then measuring the point at which the correlation drops to a certain threshold. This point corresponds to

the resolution of the image typically estimated at fixed 1/7 level. FRC has been employed to determine the resolution of super-resolution images generated by a variety of techniques, including SMLM, expansion microscopy, and cryogenic electron microscopy.

3.4 CMOS Sensors

Table 3.1. Specifications for the inspected iCMOS cameras and the reference sCMOS according to data-sheets and technical resources.

Camera	**UI-3060CP-M-GL Rev.2**	**Alvium 1800 U-158m**	**Alvium 1800 C-511m**	**ORCA Fusion**
Producer	IDS	AVT	AVT	Hamamatsu
Sensor	Sony IMX174	Sony IMX273	Sony IMX547	-
Pixel Size*	5.86 μm	3.45 μm	2.74 μm	6.5 μm
Resolution	1936 (H) × 1216 (V)	1456 (H) × 1088 (V)	2464 (H) × 2064 (V)	2304 (H) × 2304 (V)
ADC	12 bit	12 bit	12 bit	14 / 12 / 8 bit
Readout Noise	7 e^-	2.1 e^-	2.1 e^-	Fast 1.4 e^- Standard 1.0 e^- Ultra-quiet 0.7 e^-
Full Well Capacity	33000 e^-	10500 e^-	9500 e^-	15000 e^-
Saturation Capacity [e^- /μm^2]	961	882	1265	355
Quantum Efficiency [**400-700 nm**]	40-78%	45-64%	46-78%	65-80%
Technology	frontside illuminated	frontside illuminated	backside illuminated	frontside illuminated
Interface	USB 3.0	USB 3.1	USB 3.1	CoaXPress or USB 3.0
Cooling	Passive 40-50 °C	Passive 50-60 °C	Passive 50-60 °C	Active -5 °C
Price [€]**	540	316	620	~15k

* Pixel size is displayed as the square pixel side length for simplicity.

** Prices are before VAT.

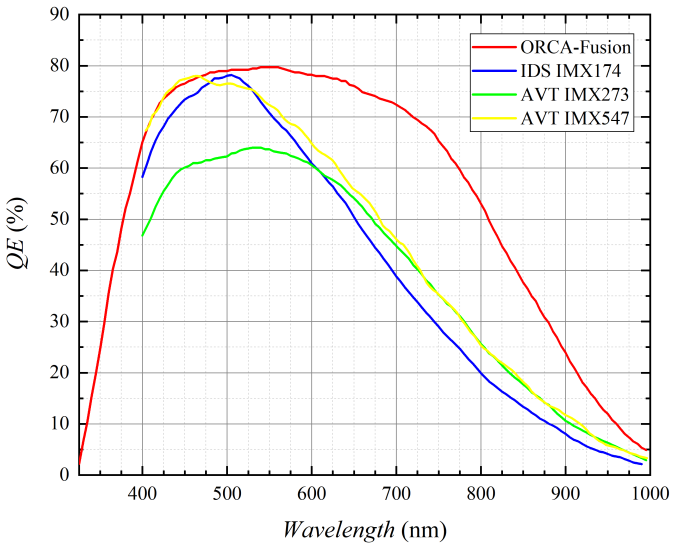

Fig. 3.2 The quantum efficiencies of the investigated CMOS cameras.

We evaluated various industrial CMOS (iCMOS) cameras that use first, second, and fourth generation PREGIUS CMOS sensors from Sony, all of which operate under the global shutter

regime. To serve as a reference, we used a Hamamatsu ORCA Fusion scientific CMOS (sCMOS) camera. Table 3.1 provides the technical specifications of the cameras we investigated. Figure 3.2 shows the claimed quantum efficiency of the CMOS cameras we evaluated, as provided by the manufacturers' data sheets. While these values are comparable to sCMOS in the 400–500 nm range, they differ in the green to IR range. Fourth-generation iCMOS provides greater QE than the first and second generations. Additionally, the fourth generation, which is back-side illuminated, provides improved sensitivity at a wide range of incidence angles. According to reports, the fourth generation retains 40% of its sensitivity at normal incidence at a 20-degree incidence angle, compared to 10% for the second generation. Therefore, we preferred to use the IMX547-based iCMOS camera for most of our experiments, along with the reference sCMOS.

3.4.1 Camera Cooling

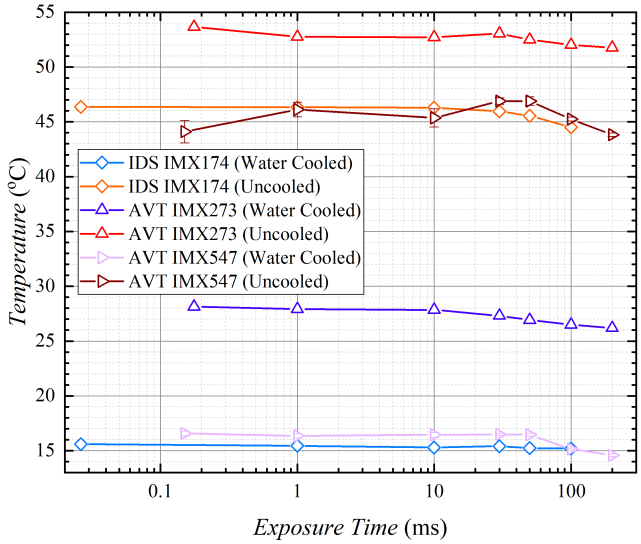

Fig. 3.3 The camera on-chip temperature sensor reading dependence on exposure time for both passive and active cooling conditions.

Table 3.1 shows that various passively cooled iCMOS cameras operate at different temperature ranges under ambient conditions. To evaluate how their characteristics vary with operating temperature, we cooled the cameras under investigation using either passive or active cooling. Each camera's body was fitted with a pair of heat-sink plates made of water blocks that served as a passive cooler. Additionally, we used a scientific water pump with active cooling/heating to regulate the camera's temperature. However, this approach may not ensure thermodynamically stable performance around the preset point due to increased heat during short exposure times or high frame rates. Figure 3.3 displays the temperature fluctuations of water-cooled (pump on) and passively-cooled (pump off) devices at different exposure times and a fixed frame rate. The temperature fluctuations remained within ∼3 °C across the range of exposure times investigated. Recently, we introduced a new cooling approach that involves a thermoelectric element in direct contact with the detector's backside. This element is controlled by a PID controller (MTDEVAL1, MTD415TE, Thorlabs), and the heat is extracted from the peltier element using a water block (AM-H4, Integrated optics) with a water temperature of ∼14.5 °C. Figure 3.4 demonstrates that using the TEC and PID controller together allows us to consistently acquire images at the same temperature, generating accurate calibration maps and reproducing the same preset configuration.

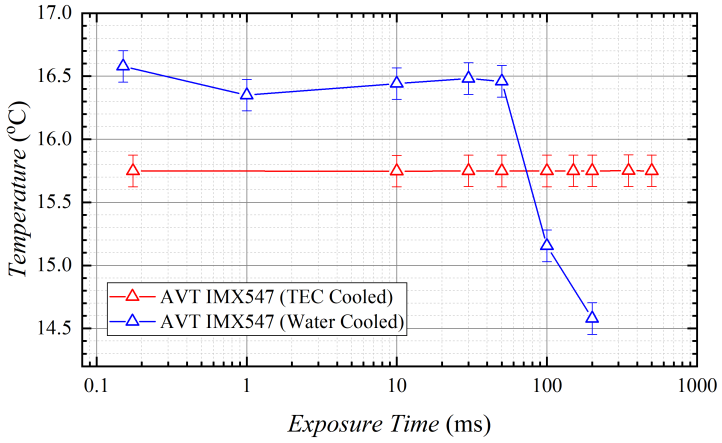

Fig. 3.4 The fourth generation iCMOS with TEC temperature stabilization compared with water cooling.

3.5 Samples

3.5.1 ATTO647N Dye Sandwich

To prepare the dye sandwich, a glass coverslip with a thickness of 170 μm (Thermo Scientific, Menzel Coverslip 24×60 mm #1.5 (0.16–0.19 mm)) was cleaned for 5 minutes using an air plasma generator (ZEPTO-W6, Diener electronic) at the highest power setting and pressure ∼260 mTorr. A double-sided sticky tape piece (3 M, 9088–200) measuring 24×60 mm was then cut with a scalpel to create a 10 × 10 mm hole in the center. The tape was attached to the cleaned glass coverslip, and a dye solution of ATTO647N-NHS ester (AD 647 N, ATTO-TEC) was prepared by diluting it to a final concentration of 2 μM in ultrapure DI water. Approximately 50 μL of the dye solution was added to the glass coverslip within the cut area.

3.5.2 GATTA-PAINT nano-rulers

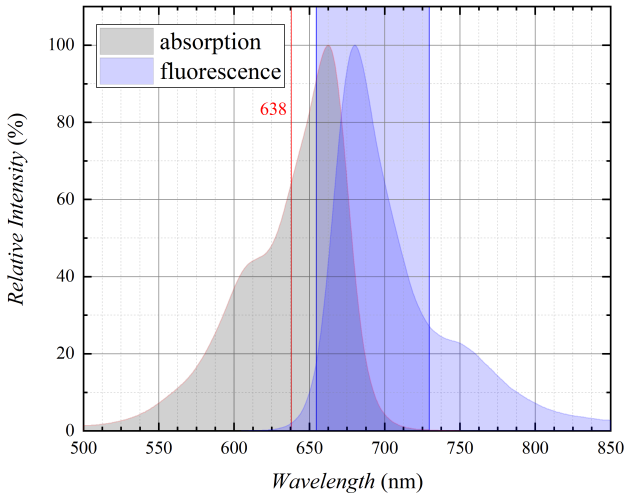

Fig. 3.5 The excitation and emission spectra of ATTO-655 used in the GATTA-PAINT nano-ruler. (Spectra source www.atto-tec.com)

We perform single-mode (SM) fiber-based TIRF-mode imaging of GATTA-PAINT nano-rulers (PAINT 80RG, GATTAquant) for localization-based super-resolution microscopy under 638 nm laser excitation. The GATTA-PAINT nano-rulers are based on DNA-PAINT technique with 3 binding sites and a mark-to-mark distance of 80 nm. The ATTO-655 fluorophore in our sample has absorption/excitation spectra as shown in Figure 3.5 and with the aid of a 692/75 nm bandpass filter, the emission is registered.

3.5.3 U-2 OS Cells with Labelled Nup96 Complexes

1. The U-2 OS-CRISPR-Nup96-SNAP clone #33 (300444, CLS GmbH) cell line was obtained from Cell Lines Service (Germany). The cells were seeded, fixed, and stained according to previously described methods [59]. The U2OS-Nup96-SNAP cells were seeded on 8 well-chambered glass coverslips (C8-1.5H-N, Cellvis) two days prior to fixation, and were grown in McCoy's 5A medium (16600082, Thermo Fisher Scientific) supplemented with 100 μg/mL streptomycin (15070063, Thermo Fisher Scientific), 100 U/mL penicillin (15070063, Thermo Fisher Scientific), 1 mM sodium pyruvate (11360070, Thermo Fisher Scientific), 1 % MEM non-essential amino acids (11140035, Thermo Fisher Scientific), and 10 % fetal bovine serum (15595309, Fisher Scientific) at 37 ^{o}C and 5 % CO_2 until they reached a confluency of about 50-70%.

2. On the day of imaging, the U2OS-Nup96-SNAP cells attached to the glass surface were initially fixed in phosphate-buffered saline (PBS; 10010023, Thermo Fisher Scientific) containing 2.4 % (w/v) formaldehyde (FA; 28906, Thermo Fisher Scientific) for 30 s. After a 3 min permeabilization step using 0.4 % (v/v) Triton X-100 (3051.2, Carl Roth) in PBS, the cells were completely fixed for 30 min in 2.4 % (w/v) FA solution in PBS. The sample was then washed twice with PBS for 5 min each time. The fixation was stopped by submerging the sample in PBS containing 100 mM NH_4Cl (5470.1, Carl Roth) for 5 min, followed by two 5 min-long washing steps in PBS. After quenching the remaining FA, a few drops of Image-iT FX Signal Enhancer (I36933, Thermo Fisher Scientific) were added to the sample and incubated for 30 min. The SNAP-tag labeled Nup96 was stained at room temperature for 2 h using benzylguanine-conjugated AF647 (S9136S, New England Biolabs) diluted to a final concentration of 1 μM in PBS supplemented with 1 μM of dithiothreitol (R0862, Thermo Fisher Scientific) and 0.5 % (w/v) bovine serum albumin (T844.2, Carl Roth). The excess unbound dye was removed by washing the sample three times with 5 min incubations in PBS.

3. For dSTORM experiments, an imaging buffer (50 mM Tris-HCl (pH 8.0, at 25 ^{o}C), 10 mM NaCl, 500 μg/mL glucose oxidase, 40 μg/mL catalase, 10 % (w/v) d-Glucose, and 143 mM 2-mercaptoethanol in H_2O) was added to the sample, which was then sealed with parafilm.

4 Results and Discussion

4.1 CMOS Characterization

We have performed a series of dark calibration measurements for the aforementioned detectors in subsection 3.4, and produced the calibration maps. Figure 4.1 demonstrates the pixel-wise linear fitting results of mean and variance dependency on exposure time. The mean fit allows us to estimate the dark current (slope) and baseline (intercept) whereas the variance allows estimating the thermal (slope) and read noise (intercept) squared. We converted the values from ADUs to photoelectrons using the gain estimate from the variance dependency on the mean discussed in subsection 3.2. The results of read noise estimate are in good agreement with specifications provided by the iCMOS manufacturers deducing the method for average gain evaluation holds. The 4th generation detector IMX547 clearly performs the best in reference with the Hamamatsu Orca-Fusion sCMOS in terms of the evaluated parameters and poses a cost-effective solution. In supplementary materials, we include table. 8.1 of mean estimated parameters over all pixels for the evaluated CMOS cameras. Also, the IMX547 camera is compared to the Hamamatsu Orca-Fusion sCMOS maps in Figure 8.1.

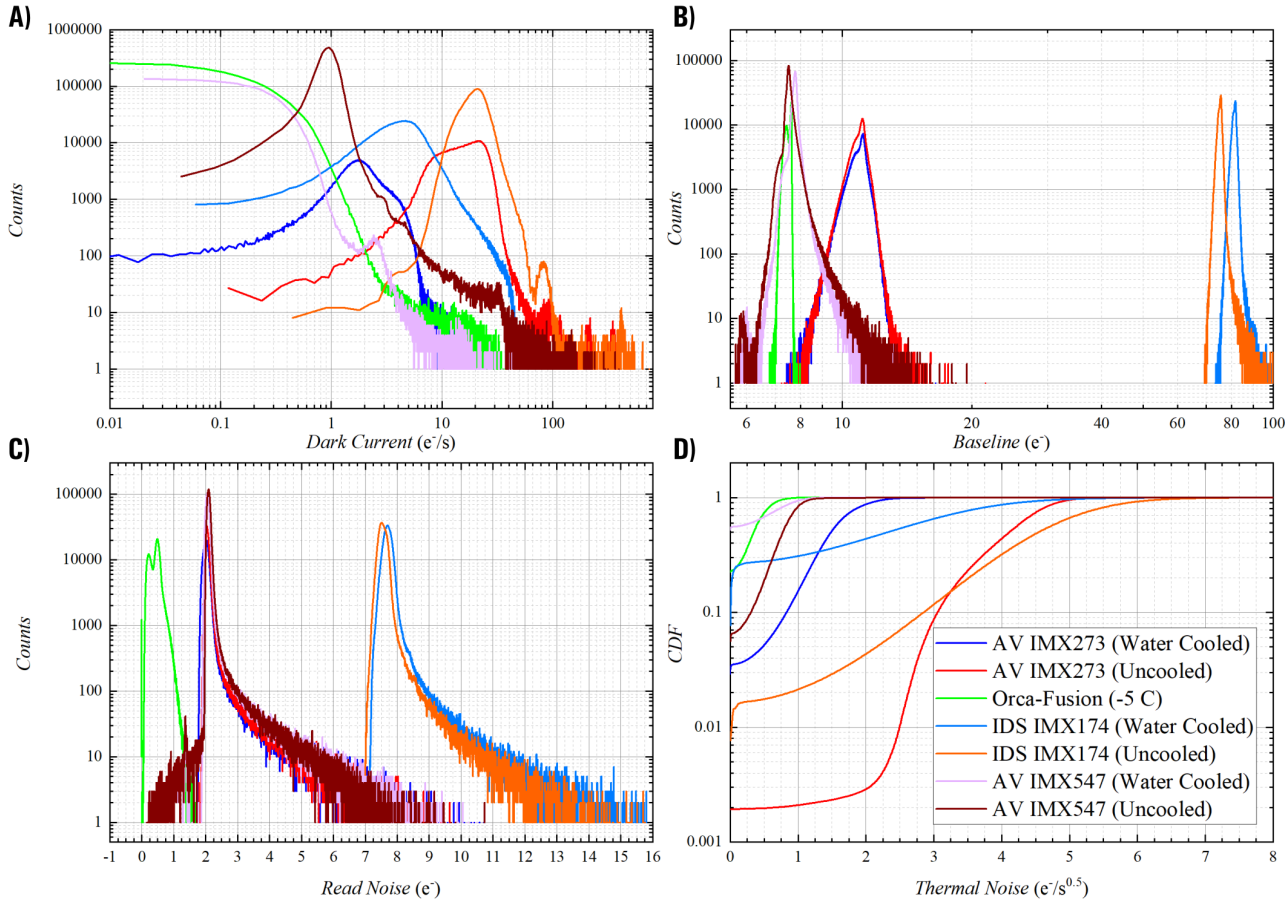

Fig. 4.1 Dark calibration pixel-wise results for the investigated CMOS cameras with dark current (A), baseline (B), read noise (C) and thermal noise (D) distributions illustrated.

We conducted additional investigations on the IMX547 detector using various cooling methods, as shown in Figure 4.2. The approach used for cooling impact pixel-wise dark current and thermal noise distributions. Among the cooling methods tested, thermoelectric cooling at 15.75 ^{o}C produced the best results, with a significant reduction in both dark current and thermal noise compared to water (∼16.5 ^{o}C) or passive cooling (∼45 ^{o}C). Mind that the detector

temperature was measured using an on-chip thermometer and recorded with each acquired image.

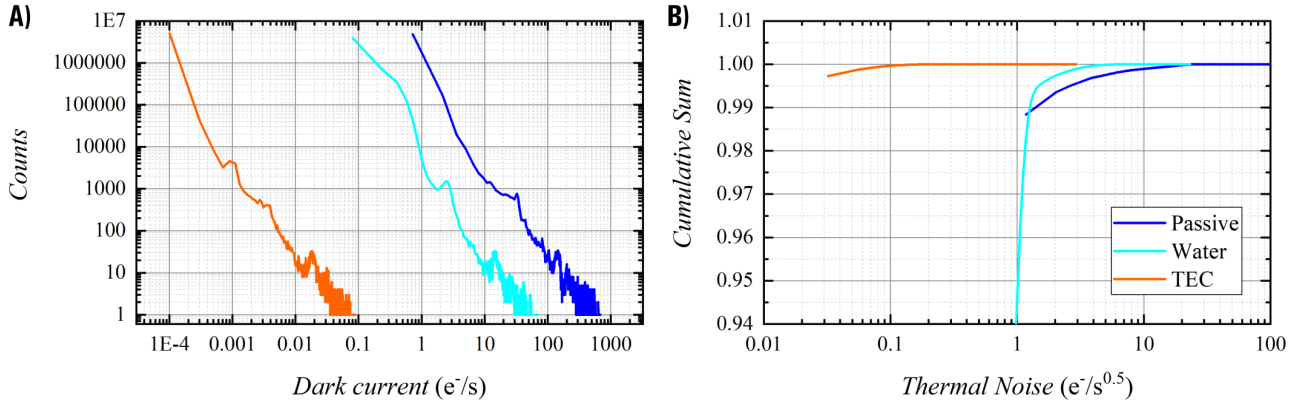

Fig. 4.2 Dark calibration pixel-wise results for the 4th gen IMX547 CMOS cameras with dark current (A), and thermal noise (B) distributions illustrated for different cooling approaches.

4.2 Excitation Profiles

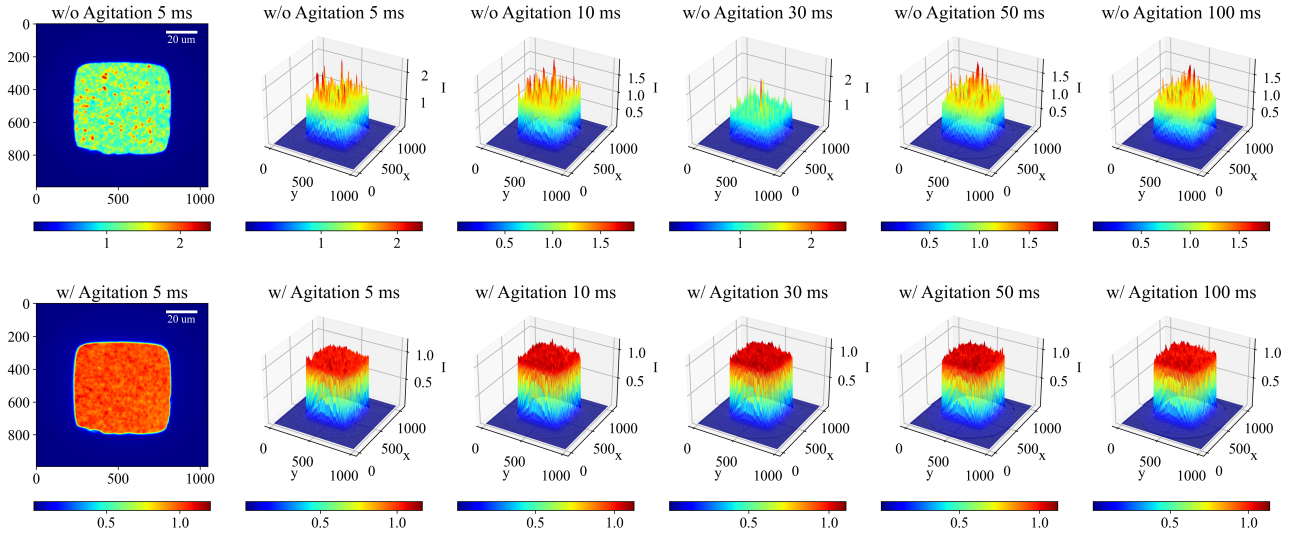

Fig. 4.3 The MMF excitation profile without and with mechanical agitation under different exposure time values.

Since a uniform illumination field is essential for fluorescence microscopy, we begin by reporting the evaluated excitation profiles. We image a "dye sandwich" between two cover slips to observe the illumination profile. To average out noise and sample inhomogeneities, we acquired 10 images at ≥ 3 locations. Due to the many modes traversing along the optical fiber, the MMF excitation results in a speckle pattern. Agitation, or mechanically shaking the MMF, produces a temporally integrated flat field that significantly reduces the magnitude of the speckle pattern. Different profiles were acquired at various exposure times, as shown in Figure 4.3 where the intensity is normalized to the mean value. Typically, when the acquisition is too fast (less than three to five milliseconds), the speckle pattern cannot be efficiently suppressed.

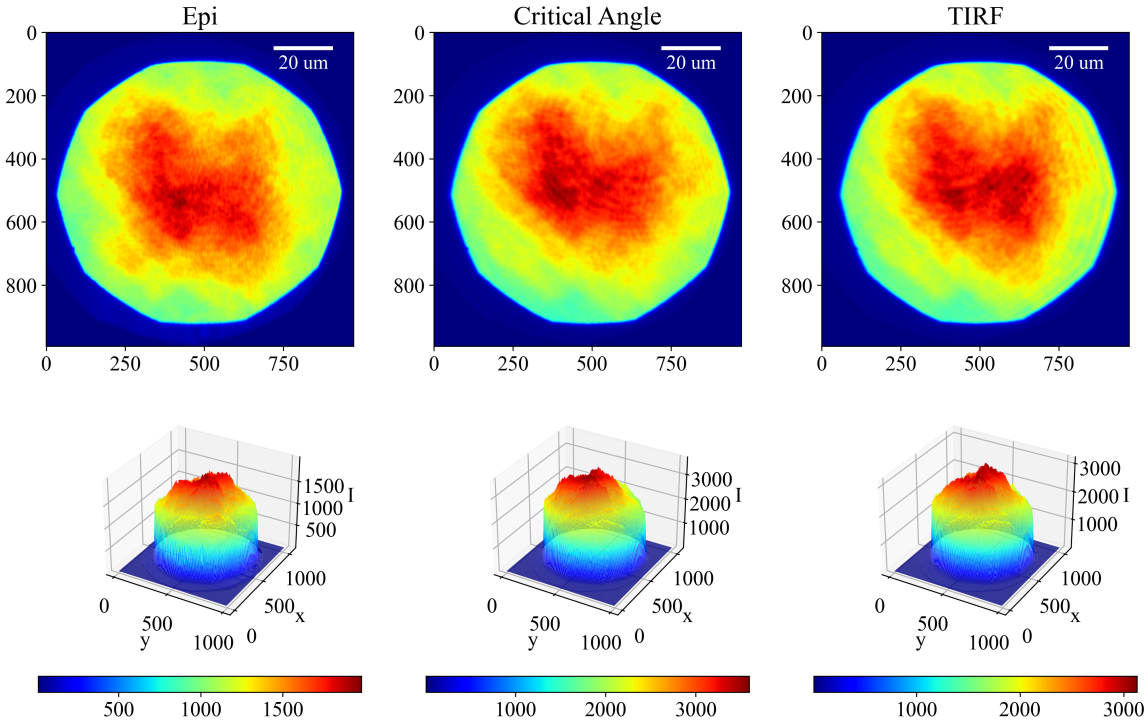

Fig. 4.4 The SMF excitation profile for normal incidence, critical angle and at an arbitrary TIRF angle.

On the other hand, the single-mode excitation has a Gaussian profile and to produce a field flatness of 15–20% one has to significantly expand the beam while restricting the illumination to the field of view using a field stop, discarding most of the laser intensity. Figure 4.4 depicts the SMF profile for *Epi*-mode, critical angle, and an arbitrary TIRF angle acquired at 50 ms exposure time and under 638 nm excitation. We further investigate the acquired MMF and SMF profiles for field unevenness by estimating the standard deviation from the mean value within the illuminated regions. Figure 4.5 (Left) demonstrates the advantages of agitation-based speckle reduction as the unevenness drops from ∼16% to below 3% resembling a top-hat illumination profile. As for SMF, Figure 4.5 (Right) displays a field unevenness within ∼16–17.5% for the three investigated modes.

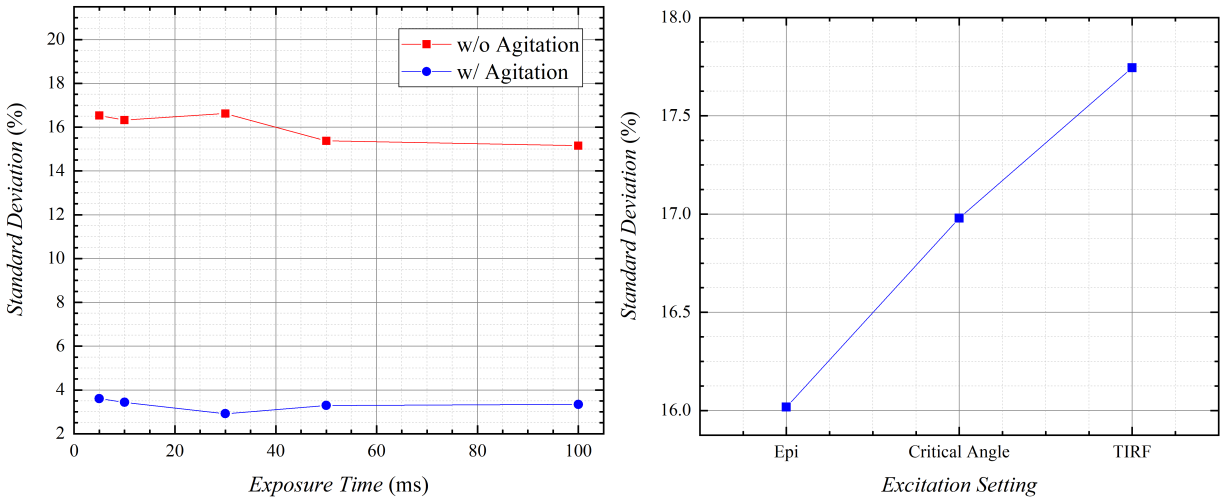

Fig. 4.5 The standard deviation of the MMF illumination without and with agitation for field flatness evaluation (Left). Similarly, the standard deviation of the SMF illumination at normal incidence, critical angle and at an arbitrary TIRF angle (Right).

4.3 Gatta-PAINT

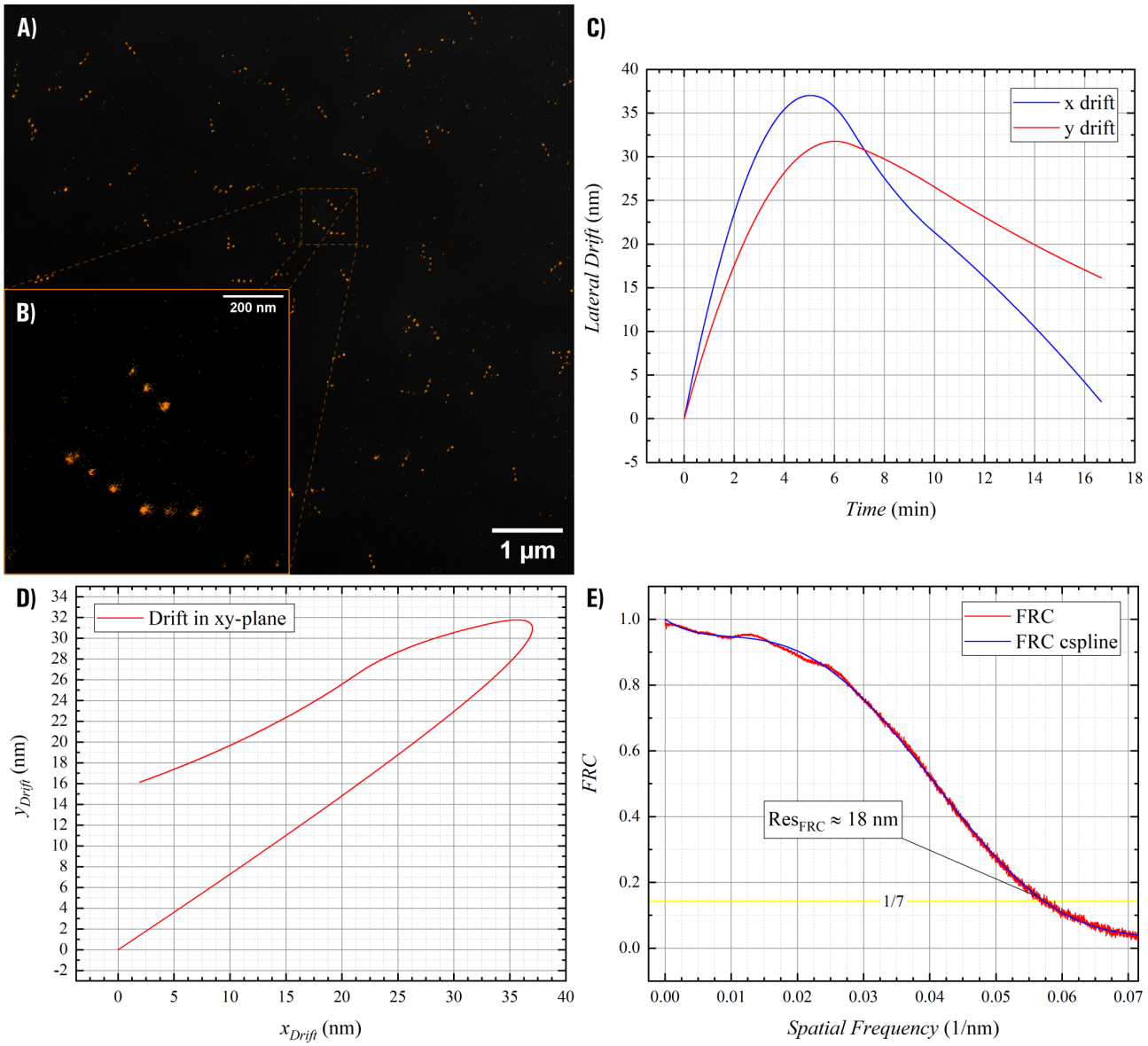

Fig. 4.6 Gatta-PAINT nano-rulers imaging results with: A) reconstructed super-resolution image overlaid on the diffraction-limited image; B) a close-up showing three nano-rulers; C) The sample drift over time estimated using two-dimensional cross-correlation; D) The lateral drift trajectory; E) FRC curve with a resolution estimate of ∼18 nm.

For benchmarking the *miEye*'s performance and resolution under TIRF excitation we chose Gatta-PAINT nano-rulers, a commercially available DNA-PAINT sample. It provides DNA-rods with three docking sites spaced 80 nm apart with a density of ~ 1 ruler/μm^2 immobilized on a cover-slip, and ATTO655-labeled imager strands. For Gatta-PAINT experiments, the SMF output (638 nm) is focused at the objective's BFP periphery to produced collimated illumination at a TIRF setting, thus excitation using the evanescent field. A 697/75 bandpass filter was used to filter the fluorescence emission. A 10,000 frame stack was acquired at 20 Hz using the iCMOS IMX547 detector with a projected pixel-size of $\sim$ 114.2 nm.

Figures 4.6A-B show a large FOV super-resolution image with resolved 80-nm-ruler-pattern and a close-up displaying three nano-rulers. The lateral sample drift estimate using 2D cross-correlation is depicted in Figures 4.6C-D, where drift over time and the XY trajectory are illustrated. Finally, the resolution is evaluated using FRC method where an ∼18 nm localization

precision is demonstrated in Figure4.6E. This demonstrates that the *miEye* provides a robust bench-top solution with high lateral resolution, an active axial drift-suppression fluctuating around 10 nm and typical lateral drift values[26].

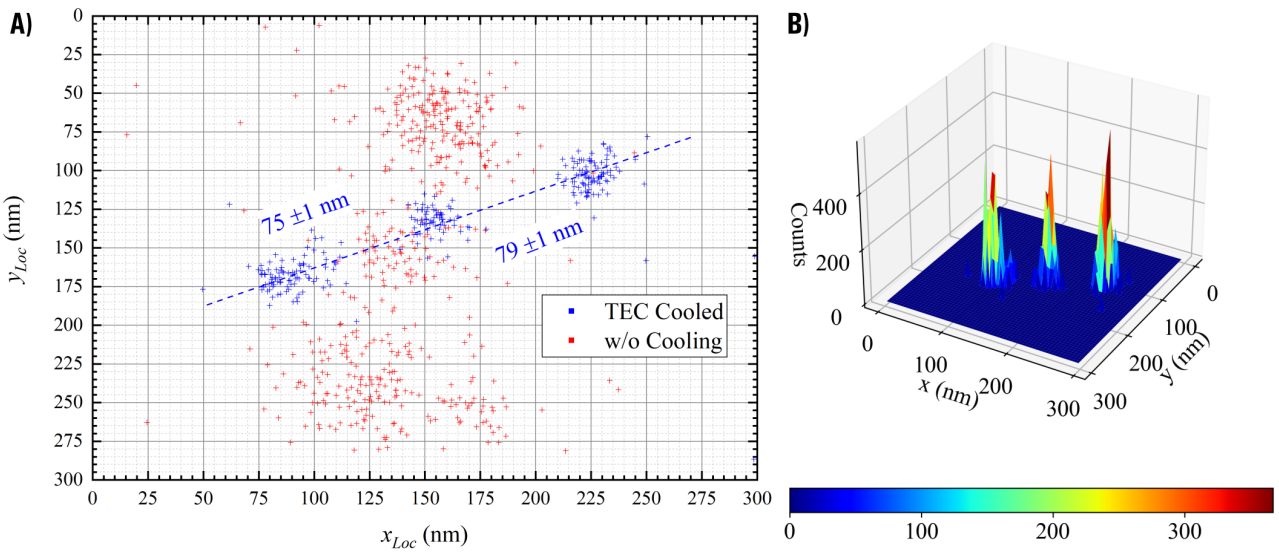

Fig. 4.7 A) Distribution comparison of nano-ruler localizations for passive and TEC cooling. B) Three-dimensional representation of the localizations 2D histogram for a single nano-ruler.

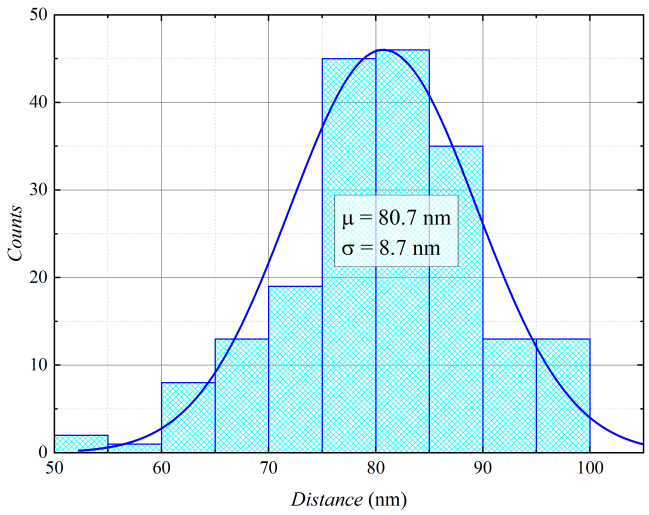

Fig. 4.8 Nearest neighbour based estimation of the distance between localized docking sites spaced within 50-100 nm apart for a wide field of view (∼70 μm^2).

We further investigated the localization precision of the nano-rulers under different cooling conditions of the iCMOS IMX547 detector, where it was passively or TEC cooled. The CMOS dark calibration maps were estimated and used when fitting localizations data for the TEC cooled setting. Figure 4.7A depicts the localization precision enhancement when the detector is cooled where localizations representing three docking sites are tightly distributed; A 3D representation of the nano-ruler 2D histogram is presented in Figure 4.7B. A refitting of the reconstructed super-resolution image allows us to evaluate the distance between docking sites within 50-100 nm in a wide field of view (∼70 μm^2) using a nearest neighbours algorithm (Figure 4.8). The results show that the mean distance is 80.7 nm with a standard deviation of 8.7 nm. Therefore, we can conclude that our two-year-old sample maintains its integrity when

stored under recommended conditions. However, our previous publication reported a ground truth resolution of 14 nm using the same sample, indicating some sample degradation[26].

4.4 dSTORM Imaging

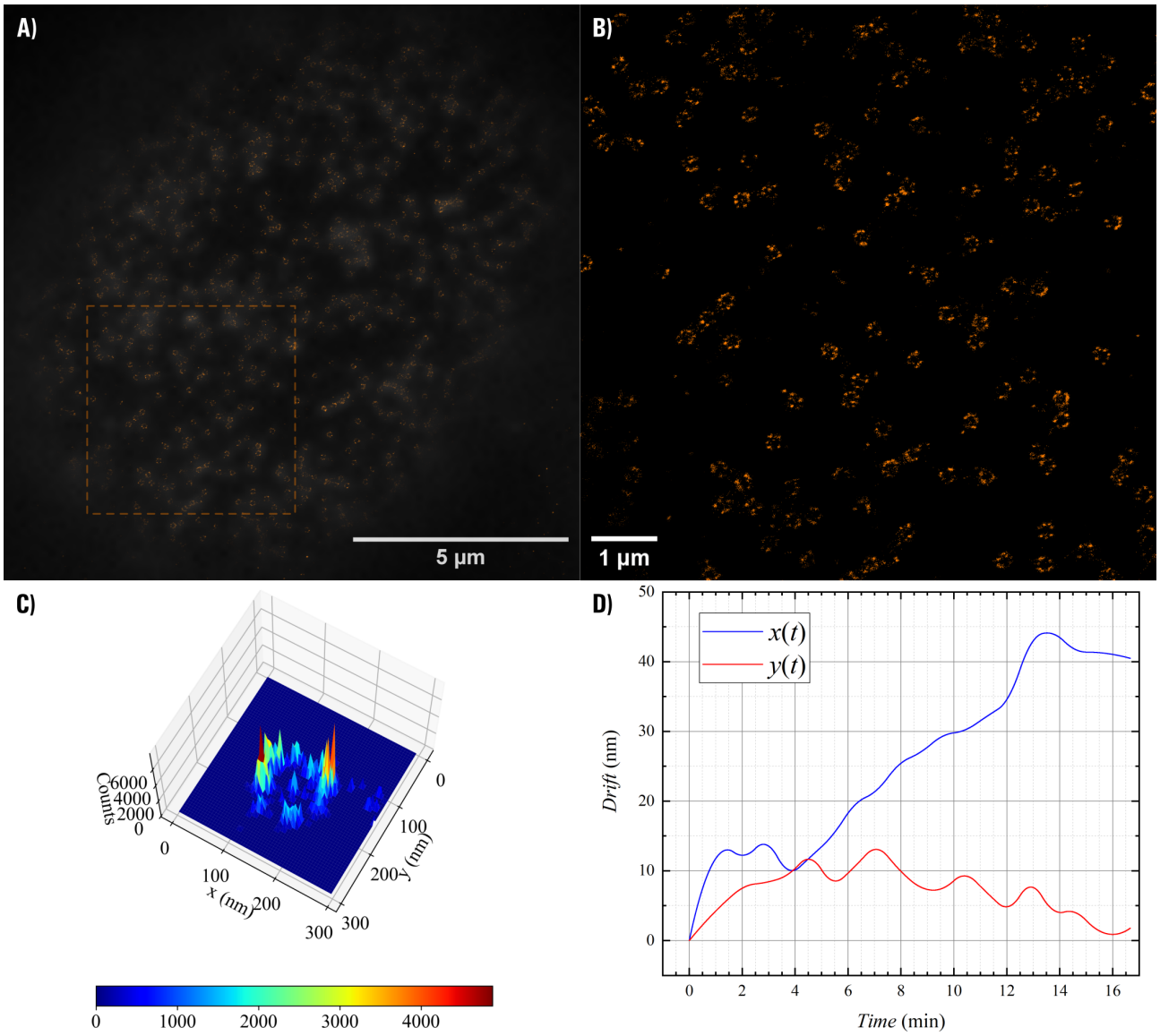

Fig. 4.9 dSTORM imaging of fluorescently labeled NPCs of fixed U2OS-Nup96-SNAP cells. A) A reconstructed super-resolution image of Nup96-SNAP-AF647-containing NPCs superimposed over an averaged image of a 20,000 frame-long diffraction-limited stack representing a U2OS cell nucleus. B) Close-up of a selected area marked by a dashed-line box in sub-figure A, with the ring-like arrangement of individual NPCs visible. C) Three-dimensional representation of the localizations 2D histogram for a single NPC. D) The sample drift over time estimated using two-dimensional cross-correlation.

In contrast with the SMF TIRF configuration, the MMF flat-field excitation allows performing SMLM slice-imaging of certain planes within a thick sample such as cells. The *miEye*'s performance under such conditions is evaluated using dSTORM imaging of nuclear pore complexes (NPCs) composed of fluorescently labelled nucleoporin Nup96-SNAP-tag conjugates in U2OS cells. Nuclear pores have recently been proven to be a versatile and biologically relevant

reference standard for benchmarking the super-resolution imaging capabilities of various microscopes[60].

For dSTORM experiments, the output end of the MMF is imaged as a conjugate plane to the sample plane. The agitator module was maintained at 1150 rpm during the whole experiment to reduce the MMF speckle pattern. The bottom flat envelope of the cell's nucleus was illuminated by a 638 nm laser with a power density of ~ 3.6 kW/cm^2. A 697/75 bandpass filter was used to filter the fluorescence emission. A 20,000 frame stack was acquired at 20 Hz using the iCMOS IMX273 detector with a projected pixel-size of ~ 129.4 nm.

Performing 2D Gaussian fitting, localization filtering and lateral drift correction on the dSTORM data allows reconstructing a super-resolution image of the fluorescently labelled NPCs in Figure 4.9A, which is overlaid onto an averaged diffraction-limited image depicting a single U2OS cell's nucleus. The ring-like structure of individual NPCs, where the nucleoporin Nup96-SNAP-AF647 conjugates reside at eight corners, is observed in a close-up of the super-resolution image (Figure 4.9B) and in a 3D representation of a single NPC (Figure 4.9C). The lateral sample drift in Figure 4.9D estimated using 2D cross-correlation falls within the expected range, where data points are grouped in 50 seconds time bins and 5 nm reconstructed pixel-size. The dSTORM experiment results finally provide a ground truth resolution of ~ 21 nm using the FRC method (Figure 4.10). This is an improvement compared to the earlier reported results (~ 35 nm) in our publication[26]. The improvement is attributed to the implementation of the iterative fitting pipeline, the *pyfit3Dcspline*, which replaced phasor-based fitting. The algorithm provides uncertainty estimates using CRLBs, which allows for the filtering of outliers.

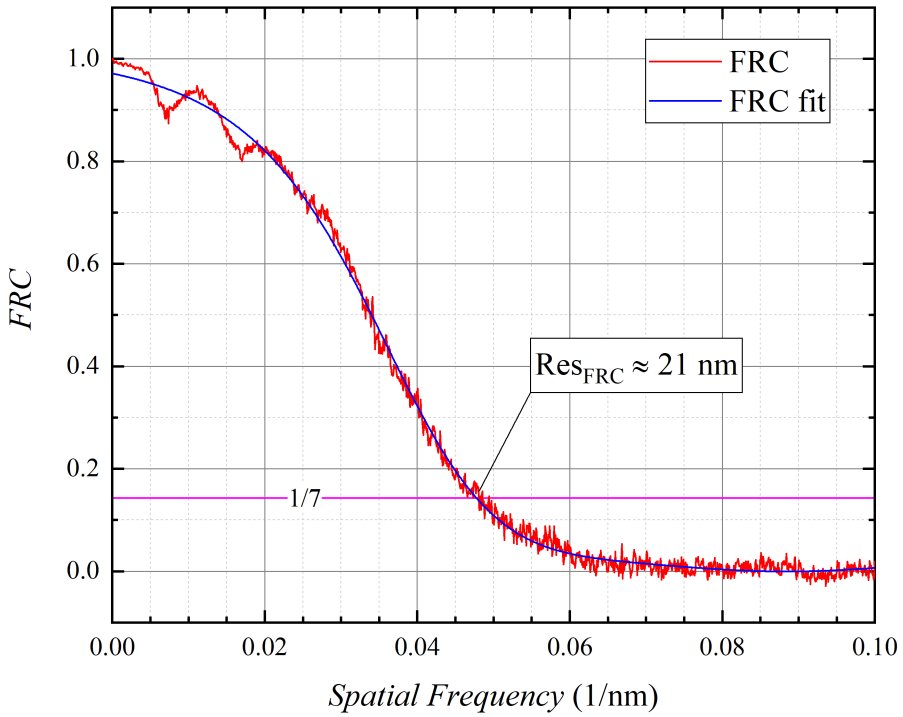

Fig. 4.10 FRC curve of the dSTORM experiment showing a resolution estimate of ~21 nm.

5 Conclusions

This study has demonstrated that the thermoelectric cooled IMX547 detector is the optimal cost-effective choice for iCMOS cameras by using dark calibration. Mechanical agitation reduced MMF excitation unevenness from 16% to below 3% standard deviation. The SMF excitation leads to a Gaussian profile causing 15-20% field unevenness upon significant beam

expansion. Gatta-PAINT nano-rulers imaging showed that the *miEye* has a high lateral resolution of 18 nm and dSTORM imaging of nuclear pore complexes in U2OS cells resulted in a lateral resolution of 21 nm with visible ring-like NPCs arrangment. The *microEye* Python package provided reliable performance for controlling hardware, acquiring data, and analyzing results.

6 Summary

English

We have introduced the *miEye* microscope, an open-source and robust bench-top SMLM platform capable of achieving high lateral resolution. The industrial CMOS characterization demonstrates significant technological improvement in the last decade, with iCMOS performance catching up with its scientific counterpart in terms of dark current, readout noise, and thermal noise. Despite their advantages, iCMOS cameras still have a limitation in their quantum efficiency for the red to IR region, which falls below 60%. This limitation can be addressed by choosing fluorophores that emit in the optimal QE region (blue→yellow). In contrast, sCMOS cameras have their quantum efficiency optimized over a wider spectral range, even reaching the IR region. The *miEye* features interchangeable excitation schemes between MMF and SMF configurations, providing flexibility in imaging various samples. Using the agitation module, we achieved a time-integrated flatness having unevenness of ∼3% with MMF, while an expanded SMF profile ranges within 15-20% unevenness. Benchmarking commercially available samples, such as the Gatta-PAINT nano-rulers, can greatly benefit implementers. It is essential to have a sample with well-known nanometer-scale features to accurately evaluate performance. By using nano-rulers, we were able to calibrate our microscope, estimate lateral resolution, and account for drift. However, it is important to note that thermal effects on iCMOS detectors can significantly impact SMLM results. For instance, when using a passively cooled detector, localizations were sparse and did not accurately represent the nano-rulers. We supplement the DNA-PAINT benchmarking results with dSTORM imaging of fluorescently labelled NPCs of fixed U2OS-Nup96-SNAP cells. The NPCs ring-like structure was observed, and the FRC resolution estimate produced a lower value than the nano-ruler results. The introduction of the iterative fitting algorithm was crucial in yielding improved dSTORM results compared to our earlier publication, where we used phasor-based fitting. It is important to note that several factors can impact the maximum achievable resolution, particularly for in-lab prepared dSTORM samples. During this study, a significant amount of time was dedicated to developing open-source software with minimal functionality from scratch. This software, called the *microEye* Python package, was used to control hardware, acquire data, and conduct analysis, resulting in a flexible and reliable pipeline. To make the software more accessible to the public, a repository was created. However, for a single individual, maintaining the repository proved to be a time-consuming and challenging task. Finally, we are currently implementing PSF shaping techniques to achieve 3D SMLM for future experiments, specifically for 3D single particle tracking.

Lithuanian

Šiame darbe mes pristatėme *miEye* - atviro kodo ir patikimą stalinę pavienių molekuliųlokalizacijos (SMLM) platformą, galinčią pasiekti aukštą skiriamąją gebą. Per pastarąjį dešimtmetį CMOS charakteristikos rodo didelį technologinį patobulėjimą, o industrinių CMOS (iCMOS) našumas pagal tamsiąją srovę, nuskaitymo triukšmą ir šiluminį triukšmą prilygsta moksliniams analogams - sCMOS. Nepaisant jų privalumų, iCMOS kamerų kvantinis efektyvumas nuo

raudonos iki infraraudonosios srities vis dar yra ribotas ir nesiekia 60%. Šį apribojimą galima pašalinti pasirenkant fluoroforus, kurie spinduliuoja optimalioje QE srityje. Priešingai, sCMOS kamerų kvantinis efektyvumas optimizuotas platesniame spektriniame diapazone, net iki IR srities. *miEye* turi keičiamas daugiamodės skaidulos ir vienmodės skaidulos konfigūracijų sužadinimo schemas, todėl galima lanksčiai žadinti įvairius mėginius. Naudodami daugiamodės skaidulos agitacijos modulį, pasiekėme, kad laike integruotas apšvietimo netolygumas su daugiamode skaidula būtų ∼3%, o išplėstinis vienmodės skaidulos profilis svyruoja 15-20% netolygumo ribose. Norint tiksliai įvertinti sistemos rezoliuciją, būtina turėti pavyzdį su gerai žinomomis nanometrinio mastelio savybėmis. Komercinių pavyzdžių, tokių kaip "Gatta-PAINT" nanoliniuotės, lyginamoji analizė gali būti labai naudinga tokių systėmų vystojams. Naudodami nanoliniuotės galėjome sukalibruoti savo mikroskopą, įvertinti šoninę skiriamąją gebą ir atsižvelgti į bandinio dreifą. Tačiau svarbu pažymėti, kad terminis poveikis iCMOS detektoriams gali turėti didelės įtakos SMLM rezultatams. Pavyzdžiui, naudojant pasyviai aušinamą iCMOS detektorių, lokalizacijos buvo retos ir netiksliai atspindėjo nanoliniuotes. DNR-PAINT nanoliniuočių lyginamosios analizės rezultatus papildėme dSTORM fiksuotų U2OS-Nup96-SNAP ląstelių fluorescenciniu žymeniu pažymėtų nukleoporinų vaizdavimu. Pastebėta į žiedą panaši nukleoporinų struktūra, o FRC skiriamosios gebos įvertinimas davė mažesnę vertę nei nanoliniuočių rezultatai. Iteracinio derinimo algoritmo įdiegimas buvo labai svarbus siekiant gauti geresnius dSTORM rezultatus, palyginti su mūsų ankstesne publikacija, kurioje naudojome fazorių pagrindu atliekamą derinimą. Svarbu pažymėti, kad didžiausios pasiekiamos skiriamosios gebos nustatymui, ypač laboratorijoje paruoštų dSTORM bandinių atveju, gali turėti įtakos keletas skirtingų veiksnių. Atliekant šį tyrimą nemažai laiko buvo skirta atvirojo kodo programinei įrangai su minimaliomis funkcijomis nuo nulio kurti. Ši programinė įranga, pavadinta *microEye* - Python paketas, buvo naudojama aparatinei įrangai valdyti, duomenims gauti ir analizei atlikti, tadd buvo sukurta lanksti ir patikima rutina. Kad programinė įranga būtų lengviau prieinama visuomenei, buvo sukurta gitHub saugykla. Tačiau vienam asmeniui saugyklos priežiūra pasirodė esanti daug laiko reikalaujanti ir sudėtinga užduotis. Galiausiai, šiuo metu diegiame PSF formavimo metodus, kad ateityje atliekant eksperimentus, konkrečiai 3D pavienių dalelių stebėjimui, būtų pasiektas 3D SMLM.

7 Acknowledgement

The Jonas Žemaitis (Engineering Sciences and Technology Sciences study groups) Presidential Scholarships for the 2022-2023 academic year.

Thanks to Meda Jurevičiūtė & Aurimas Kopūstas for dSTORM sample preparation and assistance during data acquisition.

References

[1]P. Selvin and T. Ha, *Single-molecule techniques: a laboratory manual*, Cold Spring Harbor Laboratory Series (Cold Spring Harbor Laboratory Press, 2008).

[2]J. Hohlbein, *Openmicroscopy repository*, https://github.com/HohlbeinLab/OpenMicroscopy.

[3]B. Diederich, P. Then, A. Jügler, R. Förster, and R. Heintzmann, "Cellstorm—cost-effective super-resolution on a cellphone using dstorm", PloS one **14**, e0209827 (2019).

[4]B. Diederich, Ø. Helle, P. Then, P. Carravilla, K. O. Schink, F. Hornung, S. Deinhardt-Emmer, C. Eggeling, B. S. Ahluwalia, and R. Heintzmann, "Nanoscopy on the chea (i) p", bioRxiv, 2020–09 (2020).

[5]K. Kwakwa, A. Savell, T. Davies, I. Munro, S. Parrinello, M. A. Purbhoo, C. Dunsby, M. A. Neil, and P. M. French, "Easystorm: a robust, lower-cost approach to localisation and tirf microscopy", Journal of biophotonics **9**, 948–957 (2016).

[6]C. Niederauer, M. Seynen, J. Zomerdijk, M. Kamp, and K. A. Ganzinger, "The k2: open-source simultaneous triple-color tirf microscope for live-cell and single-molecule imaging", HardwareX, e00404 (2023).

[7]J. Edwards, *Lifehack website*.

[8]A. Auer, T. Schlichthaerle, J. B. Woehrstein, F. Schueder, M. T. Strauss, H. Grabmayr, and R. Jungmann, "Nanometer-scale multiplexed super-resolution imaging with an economic 3d-dna-paint microscope", ChemPhysChem **19**, 3024–3034 (2018).

[9]K. Prakash, "Laser-free super-resolution microscopy", Philosophical Transactions of the Royal Society A **379**, 20200144 (2021).

[10]R. Strack, "The micube open microscope", Nature Methods **16**, 958–958 (2019).

[11]K. J. Martens, S. P. van Beljouw, S. van der Els, J. N. Vink, S. Baas, G. A. Vogelaar, S. J. Brouns, P. van Baarlen, M. Kleerebezem, and J. Hohlbein, "Visualisation of dcas9 target search in vivo using an open-microscopy framework", Nature communications **10**, 1–11 (2019).

[12]O. Instruments, *Rolling shutter vs global shutter scmos camera mode*, https://andor.oxinst.com/learning/view/article/rolling-and-global-shutter, [Accessed 16-May-2023].

[13]*Sony 4th Generation Pregius S – The Next Evolution of Image Sensors? - LUCID Vision Labs — thinklucid.com*, https://thinklucid.com/tech-briefs/sony-4th-generation-pregius-s/, [Accessed 16-May-2023].

[14]F. Huang, T. M. Hartwich, F. E. Rivera-Molina, Y. Lin, W. C. Duim, J. J. Long, P. D. Uchil, J. R. Myers, M. A. Baird, W. Mothes, et al., "Video-rate nanoscopy using scmos camera–specific single-molecule localization algorithms", Nature methods **10**, 653–658 (2013).

[15]R. Diekmann, K. Till, M. Müller, M. Simonis, M. Schüttpelz, and T. Huser, "Characterization of an industry-grade cmos camera well suited for single molecule localization microscopy–high performance super-resolution at low cost", Scientific reports **7**, 1–10 (2017).

[16]C. A. Schneider, W. S. Rasband, and K. W. Eliceiri, "Nih image to imagej: 25 years of image analysis", Nature methods **9**, 671–675 (2012).

[17]J. Schindelin, I. Arganda-Carreras, E. Frise, V. Kaynig, M. Longair, T. Pietzsch, S. Preibisch, C. Rueden, S. Saalfeld, B. Schmid, et al., "Fiji: an open-source platform for biological-image analysis", Nature methods **9**, 676–682 (2012).

[18]N. Sofroniew, T. Lambert, K. Evans, J. Nunez-Iglesias, G. Bokota, P. Winston, G. Peña-Castellanos, K. Yamauchi, M. Bussonnier, D. Doncila Pop, A. Can Solak, Z. Liu, P. Wadhwa, A. Burt, G. Buckley, A. Sweet, L. Migas, V. Hilsenstein, L. Gaifas, J. Bragantini, J. Rodríguez-Guerra, H. Muñoz, J. Freeman, P. Boone, A. Lowe, C. Gohlke, L. Royer, A. PIERRÉ, H. Har-Gil, and A. McGovern, *napari: a multi-dimensional image viewer for Python*, version v0.4.17rc8, If you use this software, please cite it using these metadata., Nov. 2022.

[19]J. Ries, "Smap: a modular super-resolution microscopy analysis platform for smlm data", Nature Methods **17**, 870–872 (2020).

[20]M. Ovesnỳ, P. Křížek, J. Borkovec, Z. Švindrych, and G. M. Hagen, "Thunderstorm: a comprehensive imagej plug-in for palm and storm data analysis and super-resolution imaging", Bioinformatics **30**, 2389–2390 (2014).

[21]R. Henriques, M. Lelek, E. F. Fornasiero, F. Valtorta, C. Zimmer, and M. M. Mhlanga, "Quickpalm: 3d real-time photoactivation nanoscopy image processing in imagej", Nature methods **7**, 339–340 (2010).

[22]S. Wolter, A. Löschberger, T. Holm, S. Aufmkolk, M.-C. Dabauvalle, S. Van De Linde, and M. Sauer, "Rapi d storm: accurate, fast open-source software for localization microscopy", Nature methods **9**, 1040–1041 (2012).

[23]P. Dedecker, S. Duwé, R. K. Neely, and J. Zhang, "Localizer: fast, accurate, open-source, and modular software package for superresolution microscopy", Journal of biomedical optics **17**, 126008–126008 (2012).

[24]J. Schnitzbauer, M. T. Strauss, T. Schlichthaerle, F. Schueder, and R. Jungmann, "Super-resolution microscopy with dna-paint", Nature protocols **12**, 1198–1228 (2017).

[25]A. Edelstein, N. Amodaj, K. Hoover, R. Vale, and N. Stuurman, "Computer control of microscopes using μmanager", Current protocols in molecular biology **92**, 14–20 (2010).

[26]M. N. Alsamsam, A. Kopūstas, M. Jurevičiūtė, and M. Tutkus, "The mieye: bench-top super-resolution microscope with cost-effective equipment", HardwareX **12**, e00368 (2022).

[27]*Python package microeye, a python toolkit for fluorescence microscopy that features industrial-grade cmos cameras and integrated optics laser combiner matchbox*, https://github.com/samhitech/microEye, https://pypi.org/project/microEye/.

[28]Y. Li, M. Mund, P. Hoess, J. Deschamps, U. Matti, B. Nijmeijer, V. J. Sabinina, J. Ellenberg, I. Schoen, and J. Ries, "Real-time 3d single-molecule localization using experimental point spread functions", Nature methods **15**, 367–369 (2018).

[29]R. Diekmann, J. Deschamps, Y. Li, A. Tschanz, M. Kahnwald, U. Matti, and J. Ries, "Photon-free (s) cmos camera characterization for artifact reduction in high-and super-resolution microscopy", bioRxiv (2021).

[30]E. Abbe, "Beiträge zur theorie des mikroskops und der mikroskopischen wahrnehmung", Archiv für mikroskopische Anatomie **9**, 413–468 (1873).

[31]H. Köhler, "On abbe's theory of image formation in the microscope", Optica Acta: International Journal of Optics **28**, 1691–1701 (1981).

[32]"Die lehre von der bildentstehung im mikroskop von ernst abbe", Nature **87**, 141–141 (1911).

[33]L. R. S. R. S., "Xv. on the theory of optical images, with special reference to the microscope", The London, Edinburgh, and Dublin Philosophical Magazine and Journal of Science **42**, 167–195 (1896).

[34]L. R. F.R.S., "Xxxi. investigations in optics, with special reference to the spectroscope", The London, Edinburgh, and Dublin Philosophical Magazine and Journal of Science **8**, 261–274 (1879).

[35]C. M. Sparrow, "On spectroscopic resolving power", Astrophys. J. **44**, 76 (1916).

[36]A. Nwaneshiudu, C. Kuschal, F. H. Sakamoto, R. R. Anderson, K. Schwarzenberger, and R. C. Young, "Introduction to confocal microscopy", Journal of Investigative Dermatology **132**, 1–5 (2012).

[37]D. B. Murphy and M. W. Davidson, *Fundamentals of light microscopy and electronic imaging* (John Wiley & Sons, 2012).

[38]K. N. Fish, "Total internal reflection fluorescence (tirf) microscopy", Current protocols in cytometry **50**, 12–18 (2009).

[39]O. E. Olarte, J. Andilla, E. J. Gualda, and P. Loza-Alvarez, "Light-sheet microscopy: a tutorial", Advances in Optics and Photonics **10**, 111–179 (2018).

[40]M. G. Gustafsson, "Surpassing the lateral resolution limit by a factor of two using structured illumination microscopy", Journal of microscopy **198**, 82–87 (2000).

[41]K. I. Willig, B. Harke, R. Medda, and S. W. Hell, "Sted microscopy with continuous wave beams", Nature methods **4**, 915–918 (2007).

[42]M. Leutenegger, C. Eggeling, and S. W. Hell, "Analytical description of sted microscopy performance", Optics express **18**, 26417–26429 (2010).

[43]F. Göttfert, C. A. Wurm, V. Mueller, S. Berning, V. C. Cordes, A. Honigmann, and S. W. Hell, "Coaligned dual-channel sted nanoscopy and molecular diffusion analysis at 20 nm resolution", Biophysical journal **105**, L01–L03 (2013).

[44]G. Vicidomini, P. Bianchini, and A. Diaspro, "Sted super-resolved microscopy", Nature methods **15**, 173–182 (2018).

[45]E. Betzig, S. W. Hell, and W. E. Moerner, "The nobel prize in chemistry 2014", Nobel Media AB (2014).

[46]F. Balzarotti, Y. Eilers, K. C. Gwosch, A. H. Gynnå, V. Westphal, F. D. Stefani, J. Elf, and S. W. Hell, "Nanometer resolution imaging and tracking of fluorescent molecules with minimal photon fluxes", Science **355**, 606–612 (2017).

[47]R. Schmidt, T. Weihs, C. A. Wurm, I. Jansen, J. Rehman, S. J. Sahl, and S. W. Hell, "Minflux nanometer-scale 3d imaging and microsecond-range tracking on a common fluorescence microscope", Nature communications **12**, 1478 (2021).

[48]T. Deguchi, M. K. Iwanski, E.-M. Schentarra, C. Heidebrecht, L. Schmidt, J. Heck, T. Weihs, S. Schnorrenberg, P. Hoess, S. Liu, V. Chevyreva, K.-M. Noh, L. C. Kapitein, and J. Ries, "Direct observation of motor protein stepping in living cells using minflux", Science **379**, 1010–1015 (2023).

[49]R. M. Dickson, A. B. Cubitt, R. Y. Tsien, and W. E. Moerner, "On/off blinking and switching behaviour of single molecules of green fluorescent protein", Nature **388**, 355–358 (1997).

[50]E. Betzig, G. H. Patterson, R. Sougrat, O. W. Lindwasser, S. Olenych, J. S. Bonifacino, M. W. Davidson, J. Lippincott-Schwartz, and H. F. Hess, "Imaging intracellular fluorescent proteins at nanometer resolution", science **313**, 1642–1645 (2006).

[51]S. T. Hess, T. P. Girirajan, and M. D. Mason, "Ultra-high resolution imaging by fluorescence photoactivation localization microscopy", Biophysical journal **91**, 4258–4272 (2006).

[52]S. Van de Linde, A. Löschberger, T. Klein, M. Heidbreder, S. Wolter, M. Heilemann, and M. Sauer, "Direct stochastic optical reconstruction microscopy with standard fluorescent probes", Nature protocols **6**, 991–1009 (2011).

[53]M. J. Rust, M. Bates, and X. Zhuang, "Sub-diffraction-limit imaging by stochastic optical reconstruction microscopy (storm)", Nature methods **3**, 793–796 (2006).

[54]M. Heilemann, S. Van De Linde, A. Mukherjee, and M. Sauer, "Super-resolution imaging with small organic fluorophores", Angewandte Chemie International Edition **48**, 6903–6908 (2009).

[55]A. Kuzyk, R. Jungmann, G. P. Acuna, and N. Liu, "Dna origami route for nanophotonics", ACS photonics **5**, 1151–1163 (2018).

[56]K. A. Lidke, B. Rieger, D. S. Lidke, and T. M. Jovin, "The role of photon statistics in fluorescence anisotropy imaging", IEEE Transactions on Image Processing **14**, 1237–1245 (2005).

[57]G. Bradski, "The OpenCV Library", Dr. Dobb's Journal of Software Tools (2000).

[58]K. J. Martens, A. N. Bader, S. Baas, B. Rieger, and J. Hohlbein, "Phasor based single-molecule localization microscopy in 3d (psmlm-3d): an algorithm for mhz localization rates using standard cpus", The Journal of chemical physics **148**, 123311 (2018).

[59]J. Deschamps, A. Rowald, and J. Ries, "Efficient homogeneous illumination and optical sectioning for quantitative single-molecule localization microscopy", Optics express **24**, 28080–28090 (2016).

[60]J. V. Thevathasan, M. Kahnwald, K. Cieśliński, P. Hoess, S. K. Peneti, M. Reitberger, D. Heid, K. C. Kasuba, S. J. Hoerner, Y. Li, et al., "Nuclear pores as versatile reference standards for quantitative superresolution microscopy", Nature methods **16**, 1045–1053 (2019).

8 Supplementary Materials

Table 8.1. Evaluated CMOS sensor mean values of gain, inverse gain, baseline, dark current, readout and thermal noise.

Sensor	Sony IMX174		Sony IMX273		Sony IMX547		ORCA Fusion
Cooling	w/o*	w/**	w/o*	w/**	w/o*	w/**	w/***
Gain [ADU/e^-]	0.109	0.102	0.416	0.408	0.500	0.477	0.783
Inverse Gain [e^- /ADU]	9.17	9.80	2.40	2.45	2.00	2.09	1.28
Baseline [e^-]	75.78	81.42	10.95	10.94	7.57	7.78	7.49
Dark Current [e^- /s]	22.07	6.04	19.00	2.46	1.18	0.11	0.10
Readout noise [e^-]	7.63	7.75	2.12	2.09	2.13	2.10	0.46
Thermal noise [e^- /$s^{0.5}$]	4.70	2.74	4.14	1.58	1.04	0.52	0.44

* Passive at ambient conditions. ** Water cooling. *** Active thermoelectric cooling.

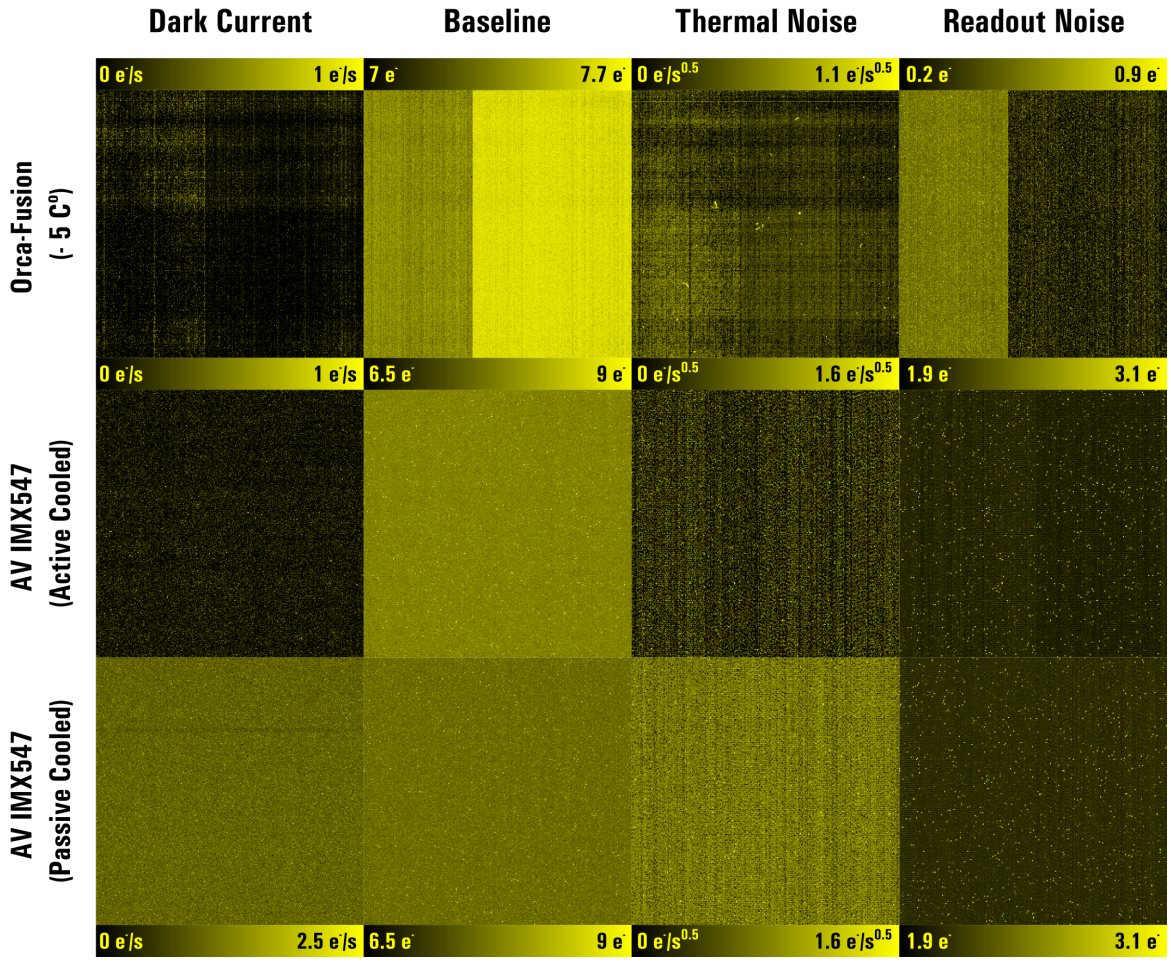

Fig. 8.1 A 512×512 cenral region of interest within the calibration maps which we have estimated using the dark measurement method for the fourth generation iCMOS camera along with the Hamamatsu sCMOS.